

THESIS FOR THE DEGREE OF LICENTIATE OF ENGINEERING

All-organic aqueous Na-ion energy storage devices

MARTIN KARLSMO

Department of Physics

CHALMERS UNIVERSITY OF TECHNOLOGY

Gothenburg, Sweden 2022

All-organic aqueous Na-ion energy storage devices
MARTIN KARLSMO

© MARTIN KARLSMO, 2022

Department of Physics
Chalmers University of Technology
SE-412 96 Gothenburg
Sweden
Telephone + 46 (0)31-772 1000

Cover: The molecular structure of Perylene-3,4,9,10-tetracarboxylic dianhydride (PTCDA).

Printed by Chalmers Reproservice
Gothenburg, Sweden 2022

All-organic aqueous Na-ion energy storage devices

Martin Karlsmo
Department of Physics
Chalmers University of Technology

Abstract

Development of all-organic aqueous energy storage devices (ESDs) is a promising pathway towards meeting the needs of technically medium/low-demanding electrical applications. These ESDs should favour low cost, low environmental impact, and safety, and thus complement high voltage and energy/power dense storage such as lithium-ion batteries. Yet, many electrode active materials dissolve in aqueous electrolytes, and most all-organic aqueous ESDs fail to deliver the claimed low cost and low environmental impact, as parts of the ESD often are overlooked.

Herein, we explore the possibilities of further developing the aqueous Na-ion battery (ASIB) electrolyte 1 m Na₂SO_{4(aq)}, with the aim to increase the electrochemical stability window and suppress active material dissolution. Moreover, electrodes with commonly used ASIB cathode/anode active materials are made more sustainable with organic binders, separators, and current collectors. Finally, we set out to assemble all-organic aqueous ESDs of exclusively commercial materials, with the aim to provide a *truly* sustainable and low-cost concept with adequate electrochemical performance.

Keywords: All-organic, battery, Na-ion capacitor, hybrid supercapacitor, battery supercapacitor hybrid, aqueous electrolyte, energy storage.

List of Papers

This thesis is based on the following papers:

- I **High-performant all-organic aqueous sodium-ion batteries enabled by PTCDA electrodes and a hybrid Na/Mg electrolyte**
M. Karlsmo, R. Bouchal, and P. Johansson.
Angewandte Chemie International Edition 60 (46), 24709-24715, 2021.
<https://doi.org/10.1002/anie.202111620>

- II **Sustainability and technical performance of an all-organic aqueous Na-ion hybrid supercapacitor**
M. Karlsmo and P. Johansson.
Submitted to *Batteries & Supercaps* 2022.

Contribution Report

- I I planned the work together with my co-authors and did all the measurements and analysis. I discussed the results with my co-authors. I wrote the first draft of the manuscript and reviewed & edited the manuscript together with my co-authors throughout the writing process.

- II I designed the study and did all the measurements and analysis. I discussed the results with my co-author. I wrote the first draft of the manuscript and reviewed & edited the manuscript together with my co-author throughout the writing process.

Additional Papers

III 2021 Roadmap for sodium-ion batteries

N. Tapia-Ruiz, A. R. Armstrong, H. Alptekin, M. A. Amores, H. Au, J. Barker, R. Boston, W. R. Brant, J. M. Brittain, Y. Chen, M. Chhowalla, Y-S. Choi, S. I. R. Costa, M. C. Ribadeneyra, S. A. Cussen, E. J. Cussen, W. I. F. David, A. V. Desai, S. A. M. Dickson, E. I. Eweka, J. D. Forero-Saboya, C. P. Grey, J. M. Griffin, P. Gross, X. Hua, J. T. S. Irvine, P. Johansson, M. O. Jones, M. Karlsmo, E. Kendrick, E. Kim, O. V. Kolosov, Z. Li, S. F. L. Mertens, R. Mogensen, L. Monconduit, R. E. Morris, A. J. Naylor, S. Nikman, C. A. O’keefe, D. M. C. Ould, R.G. Palgrave, P. Poizot, A. Ponrouch, S. Renault, E. M. Reynolds, A. Rudola, R. Sayers, D. O. Scanlon, S. Sen, V. R. Seymour, B. Silván, M. T. Sougrati, L. Stievano, G. S. Stone, C. I. Thomas, M-M. Titirici, J. Tong, T. J. Wood, D. S. Wright, and R. Younesi.

Journal of Physics: Energy 3 (3), 031503, **2021**.

<https://doi.org/10.1088/2515-7655/ac01ef>

IV Ten Ways to Fool the Masses when Presenting Battery Research

P. Johansson, S. Alvi, P. Ghorbanzade, M. Karlsmo, L. Loaiza, V.Thangavel, K. Westman, and F. Årén.

Batteries & Supercaps 4(12), 1785-1788, **2021**.

<https://doi.org/10.1002/batt.202100154>

Table of Contents

<i>Abstract</i>	III
<i>List of Papers</i>	IV
<i>Contribution Report</i>	IV
<i>Additional Papers</i>	V
<i>Table of Contents</i>	VII
1. Introduction	1
2. Batteries & hybrid supercapacitors	3
2.1 <i>Working principles and charge storage mechanisms</i>	3
2.2 <i>Sodium-ion batteries</i>	5
2.3 <i>Aqueous electrolytes</i>	6
2.4 <i>Faradaic electrode materials</i>	7
2.5 <i>All-organic aqueous energy storage devices</i>	9
3. Experimental	11
3.1 <i>Materials & cells</i>	11
3.2 <i>Physico-chemical characterization</i>	12
3.2.1 <i>Densitometry and viscometry</i>	12
3.2.2 <i>Ionic conductivity</i>	13
3.3 <i>Spectroscopy & diffraction</i>	15
3.3.1 <i>Raman spectroscopy</i>	15
3.3.2 <i>Fourier-transform infrared spectroscopy</i>	16
3.3.3 <i>Powder X-ray diffraction</i>	16
3.4 <i>Electrochemical characterization</i>	17
3.4.1 <i>Linear sweep voltammetry</i>	17
3.4.2 <i>Cyclic voltammetry</i>	17
3.4.3 <i>Galvanostatic cycling</i>	18
3.4.4 <i>Electrochemical impedance spectroscopy</i>	20

4. Results & Discussion	21
4.1 Developing the hybrid electrolyte	21
4.1.1 Guanidine salt	21
4.1.2 Magnesium and calcium salts	22
4.1.3 Prospective additives.....	26
4.2 Suppressing the dissolution of active materials	27
4.2.1 Fennac	27
4.2.2 NTP.....	30
4.2.3 PTCDA	31
4.3 All-organic aqueous energy storage devices	33
4.3.1 PTCDA//AC.....	33
5. Conclusions & Outlook	37
6. Acknowledgements	39
7. Bibliography	41

1. Introduction

Due to Europe's and United States' high energy consumption, and the rapid economic growth in China the past decades, emerging as the world's largest developing nation and energy consumer [1], the electric consumption and carbon dioxide emissions are record high (Figure 1). Meanwhile, to comply with the greenhouse gas (GHG) emission goals set by the UN by 2030 [2], western governments are phasing out fossil fuels and are pushing for an increased amount of electrification, creating an ever increasing demand for reliable and sustainable energy storage technologies.

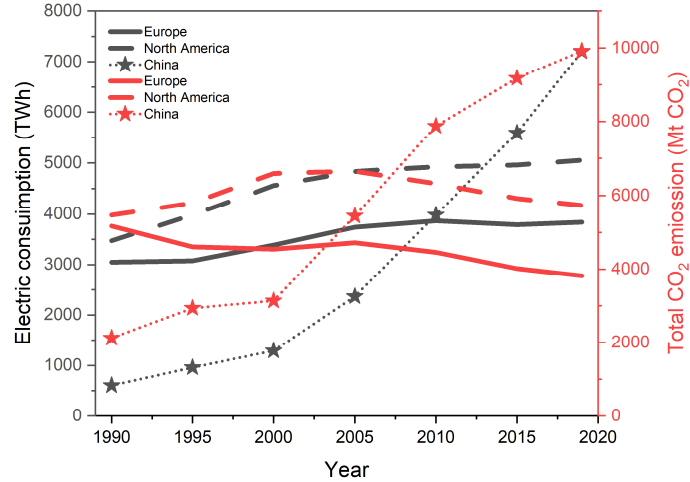


Figure 1. Electric consumption and total CO₂ emission by region from the International Energy Agency [118].

Among various energy storage systems, rechargeable batteries arguably offer the best combination of energy efficiency, energy density, flexibility and simple maintenance [3,4]. The current dominant technology, the lithium-ion battery (LIB), have since 1991 supplied energy for performance-requiring electrical applications, and its versatility has undeniably been a success-factor. However, it is also connected with high cost (while rapidly declining [5]), ethically problematic resource origins [6], and safety concerns [7,8].

In this regard, sodium-ion batteries (SIBs) and sodium-ion hybrid supercapacitors (Na-HSCs) are aspiring candidates without most of these resource issues and offer both decreased cost, improved power performance, and the former have at least the prospect of similar gravimetric energy densities [9]. By also implementing organic materials and aqueous electrolytes, a very cost effective and sustainable energy storage device can be constructed as the transition metal containing electrodes, metal current collectors, and electrolytes with toxic salts and flammable organic solvents are avoided [8,10]. This renders a device with low voltage (<2 V), but not every application requires cell chemistries optimized for high voltage and low weight, yielding energy dense devices. Some applications would in fact benefit from lower voltages, *e.g.*, Internet-of-Things (IoT) could do without built-in voltage converters if the electric source was at *ca.* 1.2-1.5 V [11]. Deviating from the state-of-the-art LIB would also be beneficial for large-scale (MWh-TWh) electrochemical energy storage installations, on- or off-grid, as a more affordable price tag and low overall environmental impact might be preferred, also with respect to the battery production and total energy throughput.

Until now, R&D efforts to accomplish functional “all-organic” aqueous batteries and HSCs, from now on referred to jointly as energy storage devices (ESDs), have almost without exception, not *really* been all-organic. Most often the ESDs have organic electrode active materials, but to fairly be promoted as all-organic, also the binder, separator, current collectors, and of course, the electrolyte should be organic. This approach would also alter the recycling and circular process. Ideally, not only are the cost and environmental impact greatly reduced as assembled, but more importantly, end-of-life (EOL) can be handled as any organic waste, *e.g.*, throw the ESD among food-leftovers or in the compost to biodegrade.

This thesis focuses on and explores the possibility of combining exclusively organic materials to construct an aqueous Na-ion ESD suited for IoT or stationary energy storage. Of course, water is not organic, neither are the salts used, but the main point pushed is the implication that these are safer, more sustainable, and less costly.

The research questions of the first paper were: Can the dissolution of the active electrode material (PTCDA) be suppressed by decreasing the amount of “free water” in the electrolyte? Can this also extend the electrochemical stability window (ESW)?

The electrode from the first paper displayed promising rate capabilities in the new electrolyte, why the second paper explored: Can we make use of this power performance and build an all-organic aqueous Na-HSC, made out of low-cost and commercially available materials?

2. Batteries & hybrid supercapacitors

The Oxford dictionary defines a battery as "A container consisting of one or more cells, in which chemical energy is converted into electric energy and used as a source of power" [12]. The principle of an ESD is to store chemical energy and be able to convert this chemical energy directly to electricity by a redox reaction. The definition above could technically include other ESDs as well, such as hybrid supercapacitors (HSCs), as they have one redox active, Faradaic electrode, instead of two, and one non-Faradaic electrode attracting charges electrostatically at the surface.

2.1 Working principles and charge storage mechanisms

The fundamental concept of rechargeable batteries and HSCs is to physically separate the anode and cathode and connect them through an external electrical circuit, enabling an electron flow, while ions are shuttled between the electrodes inside the device. To charge, an electric source is applied, and electrons will flow through the external circuit. For charge neutrality to remain, ions will migrate through the separator (in the electrolyte) from the cathode to the anode. At 100% state-of-charge (SOC) of *e.g.* a SIB, the anode has been filled, intercalated, and the cathode have been emptied, deintercalated, by cations. During discharge (Figure 2) the ions and electrons flow back in a reversed manner, performing work in the external circuit.

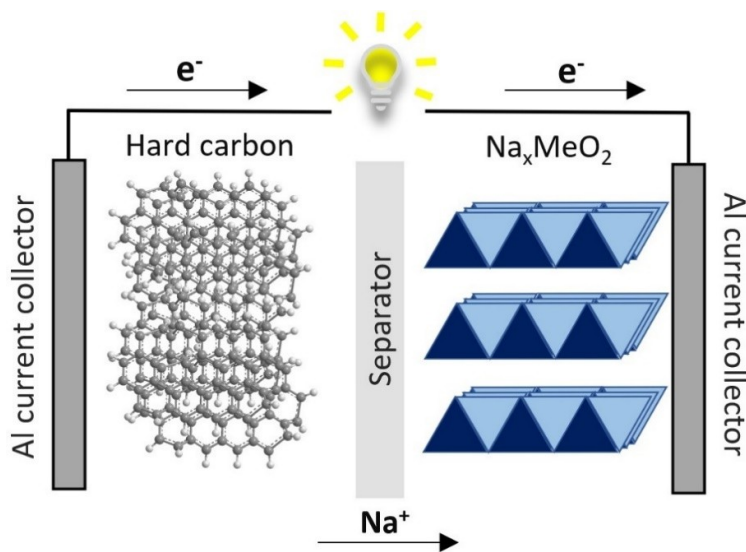
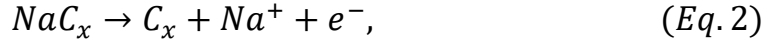


Figure 2. SIB during discharge.

The typical SIBs are assembled using hard carbon anodes, layered transition-metal oxide cathodes (Na_xMeO_2 , Me = Mn, Ti, Cu, Fe, Ni, Co *etc.*), both in contact with thin polymeric separators, wet with electrolytes made of the salt NaPF_6 dissolved in mixtures of ethylene carbonate and linear carbonates. The electrodes are coated on Al current collectors which connects and closes the external circuit. Characteristic of SIB electrodes are their ability to reversibly and without (large) structural changes insert and store Na^+ into the structure where the redox reactions happen; intercalation. This reaction would ideally occur using a NaMnO_2 cathode:



which can be divided into an oxidation reaction:



and a reduction reaction:



The amount of energy a battery cell can provide thereof relies on how many Na^+ the electrodes can accommodate and is referred to as the capacity, $Q = I \cdot t$, where I is the current and t is the discharge time. Usually the specific (gravimetric) capacity, from now on capacity, has more practical relevance, capacity per electrode mass, where NaMnO_2 is able to theoretically accommodate 244 mAh g^{-1} . Furthermore, the redox reactions experience changes in Gibbs free energy (ΔG) and have corresponding electrochemical potentials, E_{cathode} and E_{anode} , according to:

$$\Delta G = -nFE_{\text{cell}} = -nF(E_{\text{cathode}} - E_{\text{anode}}), \quad (\text{Eq. 4})$$

where E°_{cell} is the theoretical cell voltage and often measured vs Na^+/Na . The energy (E) of the cell is then a function of voltage and capacity,

$$E = \int_0^Q E_{\text{cell}}(q) dq. \quad (\text{Eq. 5})$$

The convention is also for energy to be given as the energy per mass or volume, *i.e.* specific energy or volumetric energy density, where *e.g.* commercial Na-ion batteries by Faradion hold 160 Wh kg^{-1} and 290 Wh l^{-1} at the cell level [13].

HSCs on the other hand make use of the fast double layer charge storage mechanism [14] at one of the electrodes. During operation, either by extraction or insertion of electrons, the electrode surface becomes charged, and oppositely charged electrolyte ions will form a layer to compensate for this. According to the well-established Stern model [15] (Figure 3), developed from prior models by Helmholtz and Guoy-Chapman, an inner compact Stern layer and an outer diffuse layer will form and screen the charges of the surface. So far, this is considered the most accurate model and capacitances for flat surfaces can be gathered with high accuracy.

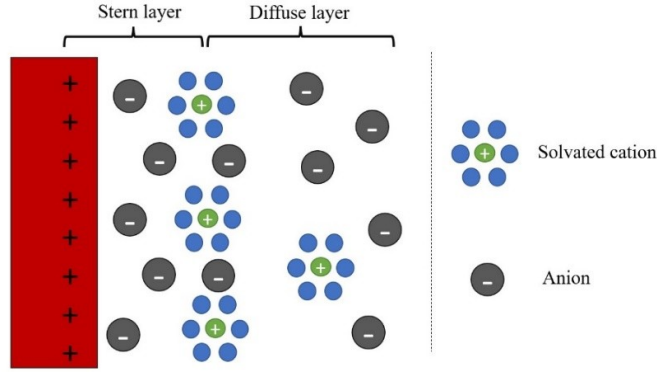


Figure 3. Stern model.

The performance measures for HSCs are calculated slightly different as compared to batteries. Here, specific capacitance (C_{sp}) can be, and are sometimes used, instead of capacity,

$$C_{sp} = \frac{I}{m \left(\frac{dV}{dt} \right)}, \quad (Eq. 6)$$

where I is the discharge current, m is the mass (often of the anode and cathode active materials), V is the voltage, and t is the time. The specific energy densities and power densities are thereafter calculated as follows,

$$E = \frac{C_{sp} \cdot \Delta V^2}{7.6}, \quad (Eq. 7)$$

and

$$P = \frac{E}{\Delta t} \cdot 3600, \quad (Eq. 8)$$

where ΔV is the discharge voltage range and Δt is the discharge time in seconds. The double layer mechanism is of course limited to the electrode surface, which limits the amount of charges stored and thus the energy density, but it opens up the possibility for high power densities if paired with a redox active electrode with fast charge-storage kinetics. This configuration can therefore achieve both relatively high energy densities and power densities, as both Faradaic and non-Faradaic processes are employed simultaneously [16].

2.2 Sodium-ion batteries

The research field of next generation batteries is ever increasing and a substantial amount of work has been put into the 6th most abundant element in the crust of Earth, sodium [17,18]. SIBs were originally studied alongside LIBs in the 1970s and 1980s, but were more or less abandoned the coming three decades due to the rapid advances of LIBs. During the past decade however, SIBs have been picked up again due to an increased climate awareness and in pursuit of more cost-effective energy storage solutions. Several companies, including Altris, Faradion, Tiamat, Novasis Energies, and Natron Energy are developing SIBs [9,19],

and recent years have even demonstrated their practical viability with E-bikes, Sydney Water's Bondi Sewage Pumping Station, and a 30 kW/100 kWh energy storage power station in China [20,21].

SIBs offer better power densities (1000 *vs. ca.* 400 W kg⁻¹), the prospect of similar gravimetric energy densities (160 *vs. ca.* 250 Wh kg⁻¹), but lower volumetric energy densities (290 *vs. ca.* 700 Wh l⁻¹) as compared to LIBs [9]. The larger Na⁺ ($r_{\text{Na}^+} = 1.02 \text{ \AA}$, $r_{\text{Li}^+} = 0.76 \text{ \AA}$) also makes insertion/extraction more difficult, and the host electrode can undergo significant volume changes which can lead to structural degradation that reduces the cycle life and performance of the battery [22]. However, the advantages of SIBs are manifold; mineral resources containing sodium are practically unlimited, geographically well distributed and therefore attainable at low cost [10]; neither natural graphite nor cobalt are needed for the electrodes; SIBs can be made with Al CCs on both sides; valuable knowledge and infrastructure gathered for LIBs can easily be carried over to SIBs [23]. As a consequence, a considerable amount of intercalation materials have been explored, and at the cathode side layered transition-metal oxides, polyanionic materials, Prussian Blue Analogues (PBAs), and organic materials have proven to perform well [9]. At the anode side, hard carbon is the most common, but Ti-based oxides, different alloys, organic materials, and 2D transition-metal dichalcogenides have also been applied. Finally, a standard SIB electrolyte has not yet been established, but apart from the LP30 sodium analogue (1 M NaPF₆ in EC/DMC), some promising salts include NaTFSI with reduced toxicity and high thermal stability, as well as NaBOB when combined with the non-flammable trimethyl phosphate (TMP) [24].

2.3 Aqueous electrolytes

The commercial non-aqueous electrolytes are, however, costly, highly flammable, and hazardous with their ability to form toxic gases [8,25]. The synthesis using/producing fluorine itself is also non-environmentally friendly, costly, and potentially dangerous [7,26]. Thus, diverging from these solvents and salts would greatly benefit the ESD in terms of cost and sustainability. Ideally, a liquid electrolyte also features low viscosity, high ionic conductivity, wide ESW, the ability to wet the separator, and an inertness while in contact with all cell components. Aqueous electrolytes at least exhibit the former two, due to the unique dielectric and fluid properties of water, and some 15 years ago aqueous SIBs (ASIBs) emerged.

As of today, 1 M Na₂SO_{4(aq)} is the most commonly used electrolyte for ASIBs with an ESW of *ca.* 2 V, a high ionic conductivity (*ca.* 100 mS·cm⁻¹), a low viscosity (*ca.* 1.2 mPa·s), low inherent materials cost, high safety, and compatibility towards many electrode materials [27]. For an optimal utilization of the ESW, the redox potential of the electrode materials should lay within or near the electrolysis potential of water to avoid the hydrogen evolution reaction (HER) and the oxygen evolution reaction (OER). Historically, this has rarely exceeded that of pure water (1.23 V), limiting both the cell energy density and the applicable electrode materials. Not all applications, however, require high cell voltages and energy/power density. For large-scale energy storage and IoT, aqueous ESDs would actually be preferred as they offer a low cost, eco-friendliness, and high safety [27].

Nevertheless, the battery community has recently shifted from the typical 1 M concentration with a new concept introduced 2015 by Suo *et al.* known as "water-in-salt" electrolytes (WISEs) [28]. Their definition constitutes that the dissolved salt outnumbers water by both volume and mass, and this new strategy has been highly effective with aqueous batteries operating >3 V [29]. By adding more salt, most of the water molecules coordinate in the first ion solvation shell, shifting the electrochemical stability and the salt anion reduces before the water molecules [30].

As the water concentration decreases, naturally the solubility of different species also decreases; WISEs have therefore also proven to be an effective way of suppressing active material dissolution, by decreasing the "free water"¹ in the electrolyte [31,32]. Active material solubility has been a considerable drawback as a large number of intercalation compounds suffer from dissolution in aqueous electrolytes. Furthermore, many organic active materials only facilitate redox reactions in organic electrolytes [33,34]. Looking back, the 1 M tradition originated from non-aqueous electrolytes almost always having the highest ionic conductivity at that concentration, a balance between number of charge carriers and the viscosity of the electrolyte [35], which does not necessarily apply to aqueous electrolytes.

Yet, WISEs are intrinsically based on high salt concentrations, and expensive salts might limit this new pathway. Many popular salts also contain fluorine or perchlorate, defeating the original purpose of aqueous batteries being low cost, safe, and environmentally benign [36]. There are only a few examples of batteries based on fluorine-free, cheap and green WISEs/water-in-bisalts (WIBEs), such as Han *et al.*'s and Lukatskaya *et al.*'s 40 m WIBEs (32 m KAc + 8 m LiAc and 32 m KAc + 8 m NaAc) [37,38]. The alkaline environment caused by the AC anion is however not compatible with PBAs, causing instability and capacity fading [38]. Therefore, a new electrolyte concept is needed that addresses all the issues of material dissolution, narrow ESWs, and costly salts.

2.4 Faradaic electrode materials

At the cathode side, some promising options which can reversibly accommodate Na^+ are; polyanionic compounds containing $(\text{XO}_4)^{n-}$ ($\text{X} = \text{P}, \text{S}, \text{Mo}, \text{etc.}$) units, they have open 3D frameworks that allow fast conduction; Mn-based oxides with tunnel networks; and PBAs with their unique open framework-structures and often high redox potentials (Figure 4).

One of the earliest ASIB/Na-HSC cathodes, $\text{Na}_{0.44}\text{MnO}_2$, was investigated by Whitacre *et al.* in 2010 [39] with a relatively low capacity (45 mAh g^{-1}), but the AC// $\text{Na}_{0.44}\text{MnO}_2$ HSC had an excellent cycling stability. Another similar HSC, AC// λ - MnO_2 rendered 80 mAh g^{-1} and outstanding capacity retention (no capacity loss over 5000 cycles) [40]. Furthermore, Zhang *et al.* investigated the polyanionic $\text{Na}_3\text{V}_2(\text{PO}_4)_3$, achieving 73 mAh g^{-1} , and 36 Wh kg^{-1} with a $\text{NaTi}_2(\text{PO}_4)_3$ (NTP) anode [41]. Many vanadium compounds, however, suffer from dissolution of V, resulting in large irreversible capacity losses, leading to poor cycling stability [42]. This is also the case for $\text{Na}_2\text{VTi}(\text{PO}_4)_3$, able to act as both cathode and anode

¹ Water molecules only interacting with other water molecules.

due to the V^{4+}/V^{3+} and Ti^{4+}/Ti^{3+} redox couples [43]. $Na_3MnTi(PO_4)_3$ on the other hand achieved 58 mAh g^{-1} and 40 Wh kg^{-1} in a symmetric configuration, and had 98% capacity retention after 100 cycles [44].

PBAs often display high capacity, high redox potential, and good cycling stability [45]. The larger Na^+ ions fit better in the PBAs' voids (compared to Li^+), which facilitates good power performance [46], making them suitable for HSCs. To name a few, PBAs based on Ni, Co, Cu, and NaCo have been investigated, reaching capacities $<120 \text{ mAh g}^{-1}$ [47]. However, as aqueous ESDs are meant to be low-cost and environmentally friendly alternatives, transition-metal cathodes are not ideal. Instead, iron-based PBAs render *ca.* 110 mAh g^{-1} split over two redox plateaus [48,49]. Reaching the high potential plateau is, however, problematic, as it is situated outside the ESW of most aqueous electrolytes, requiring HSC scan rates ($>500 \text{ mA g}^{-1}$ or $>10C$) to be utilized.

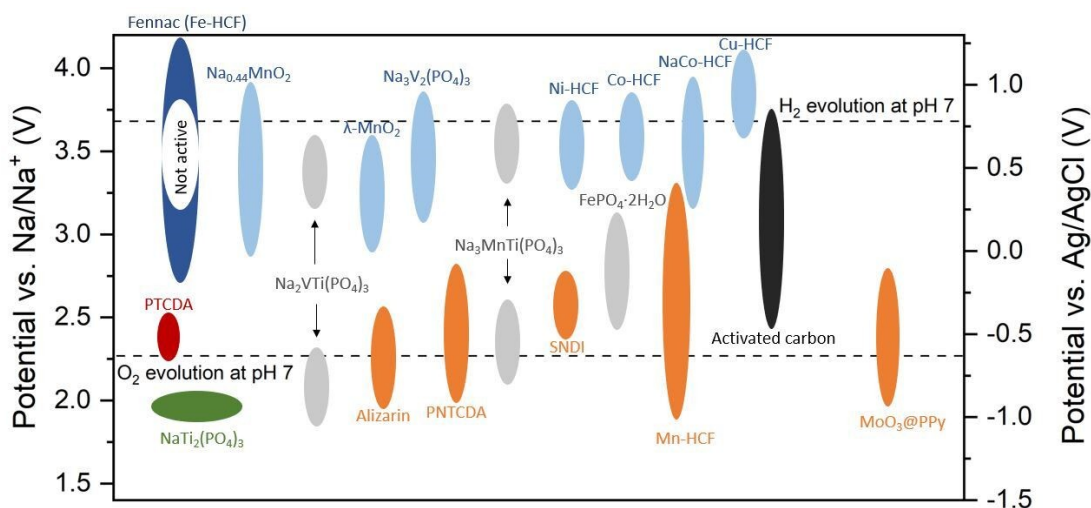


Figure 4. A selection of electrode materials for aqueous Na-ion ESDs.

The anodes for ASIBs have almost without exception been based on NTP as active material [50]. The redox potential of NTP ($-0.9 \text{ V vs. Ag/AgCl}$) is almost perfect, and due to its high capacity ($120\text{-}130 \text{ mAh g}^{-1}$) it is the state-of-the-art ASIB anode, where further advances have been relatively scarce [51]. Pristine NTP has poor electrical conductivity and cycling stability, but adding a carbon coating improves both [52]. A NTP/C composite//AC HSC *e.g.* delivered 32 Wh kg^{-1} and 88% capacity retention after 2000 cycles [53]. However, the potential of NTP is slightly below the reduction limit of most ASIB electrolytes, and it requires an oxygen-free environment to avoid oxidation and severe capacity fading [54,55].

Apart from NTP, metal oxide composites like $MoO_3@PPy$ (33 mAh g^{-1}) [56], Mn-based PBAs (33 mAh g^{-1}) [57], and different organic materials have been applied. The latter includes the biomolecule alizarin and several polyimides [34,42]. Yet, none of them offer any appreciable capacity in combination with long-term stability at battery C-rates. There is one exception, PNTCDA, which was applied with a $17 \text{ m NaClO}_{4(aq)}$ WISE and delivers 133 mAh g^{-1} [58]. When coupled with porous carbon microspheres, the all-organic aqueous Na-HSC displayed record high energy/powder densities (65 Wh kg^{-1} , 20 kW kg^{-1}) and 86% capacity

retention after 1000 cycles. The authors do, however, attribute the excellent performance of to the high electrolyte concentration, which increases the Na^+ activity and thereby enhances the reaction kinetics, as PNTCDA in 5 m and 10 m $\text{NaClO}_{4(\text{aq})}$ did not perform as well. A similar organic molecular structure, β -perylene-3,4,9,10-tetracarboxylic dianhydride (β -PTCDA), was originally studied as a LIB cathode [59], and later on also in SIBs where it reversibly intercalates two Na^+ [60]. α -PTCDA (from now on PTCDA), with slightly different crystal structure [61], has also been used as anodes in aqueous K-ion, Mg-ion, and H_3O -ion batteries [31,62,63]. For the former, β -PTCDA was witnessed to extensively dissolve in its reduced state, and as a remedy, a 30 m KFSI WISE was applied, resulting in significantly improved capacity retention [31]. Herein, we try to tackle the dissolution issue of PTCDA in a similar manner by developing the 1 m $\text{Na}_2\text{SO}_{4(\text{aq})}$ electrolyte, to enable it in ASIBs/Na-HSCs (I).

2.5 All-organic aqueous energy storage devices

The final step on the sustainability ladder, after the use of sodium and aqueous electrolytes, is to limit all other parts of the ESD to organic materials, preferably entirely/mainly from renewable resources [64]. Organic materials have inherent advantages as they offer high stability, low cost, structural designability, and biodegradability [65,66]. All-organic batteries would alleviate most of the environmental and ethical concerns of the commercialized LIBs, and this has led to organic electrode active materials being explored using both non-aqueous [10] and aqueous [67] electrolytes. So far, many organic SIB electrodes fail to deliver their redox capacities with, or they detrimentally dissolve into, aqueous electrolytes [31,33], but some exceptions include the already mentioned biomolecule alizarin and polyimides.

The unique selling point of HSCs are their ability to provide both a high power density *and* relatively high energy density, where the former originates from the non-Faradaic surface interactions of the capacitive electrode. In a patent from 1954 H.I. Becker describes what will become the most commonly used non-Faradaic electrode material for electric double layer capacitors (EDLCs); AC [68]. The success of AC is a result of its extremely high specific surface area ($<4000 \text{ m}^2 \text{ g}^{-1}$), high conductivity, low cost, and compatibility with most electrolytes [69]. EDLC charge storage mechanism does, however, limit the capacity to *ca.* 30-45 mAh g^{-1} [53,70], why HSCs are not suitable for energy density requiring applications such as electric vehicles.

Other carbon based non-Faradaic electrodes have been applied to create EDLCs/HSCs, but they are rarely commercially available due to intricate synthesis routes. This is also true for the active materials in almost all the all-organic aqueous ESDs that have been reported so far (Table 1). The better performing also have binders, separators, and current collectors (except carbon paper) that are not so “green” either. Frankly, there are no all-organic aqueous Na-ion ESD comprised of commercial materials, HSC or battery, no less a device acknowledging all cell components. If realized however, an all-organic aqueous Na-ion ESD would provide safe, sustainable, low-cost, and possibly biodegradable energy storage. We explore this promising concept by assembling all-organic aqueous Na-HSCs based on PTCDA and AC (II).

Table 1. ESDs – batteries and HSCs.

ESD [ref]	Cathode	Anode	Binder	Separator	Current collector (s)	Electrolyte	Energy density (Wh kg ⁻¹)	Power density (kW kg ⁻¹)	Cell voltage (V)	Capacity retention (%); cycles (#); rate (A g ⁻¹)
Hybrid [58]	Carbon microspheres	PNTCDA	PTFE	Glass fiber	Stainless steel grid	17 m NaClO ₄	65	20.0	2.0	86; 1000; 1
Hybrid [71]	ATA polymer	PDI-Ph polymer	PVDF	-	Carbon cloth	30 m NH ₄ Ac	16.5	0.72	1.9	63; 5000; 0.4
Hybrid [66]	Methylene blue@GO	Polyimide	PTFE	Anion-exchange membrane	Ti mesh	1 M H ₂ SO ₄ and 1 M (NH ₄) ₂ SO ₄	49	19.0	1.9	83; 10000; 5
Battery [72]	TCHQ	AQ	PTFE	-	Au mesh	0.5 M H ₂ SO ₄	22	-	1.0	-
Battery [73]	Polytriphenyl amine	PNTCDA	PTFE	-	Ti and Ni	21 m LiTFSI	53	32.0	2.1	85; 700; 0.5
Battery [74]	C-L	C-PI	CMC	Celgard 5550	SS	PAAK	16	6.8	1.7	~65; 2500; 0.5
Battery [75]	Polycatechol	Polyimide	PVDF	Glass fiber	Carbon paper	2.5 M LiNO ₃ + 0.25 M H ₂ SO ₄	81*	348.0*	1.0	80; 1000; 5
Battery [76]	Tiron	AQDS	-	Glass fiber	Ti foil	1 M H ₂ SO ₄	29	~0.4	0.9	70; 600; 5C
Battery [77]	PTMA polymer	NTCDA-EDA polymer	PTFE	-	-	1 M (NH ₄) ₂ SO ₄	51	15.8	1.9	86; 10000; 5
Battery [78]	PTAm	PTPM	-	-	ITO	0.1 M NaCl	-	-	1.7	80; 2000; 60C
Battery [79]	PLA-PTAm	SBS-PAQE	-	PLA	-	3 M NaCl	-	-	1.6	-
Battery [80]	C/DHB	C/AQ	-	Nafion	AC and Ti	1 M H ₂ SO ₄	10	6.3	1.2	-

* Calculated based on the weight of the redox-active unit in the copolymer.

3. Experimental

As an experimentalist in battery science, naturally, experimental techniques make up a main part of my work. This chapter sets out to describe the materials & cells used and created, as well as the physico-chemical, electrochemical, and material analyses used to characterize the properties of the electrolytes, the electrode materials and finally, the assembled cells.

3.1 Materials & cells

The electrolytes were prepared in a straightforward way by mixing a weighed amount of salt and ultra-pure water (Millipore® Direct-Q® Purification, 18.2 MΩ·cm at 25°C) in magnet stirred vials, at *ca.* 40-50°C to ensure a fast dissolution. They were thereafter cooled by ambient air to room temperature. The dual salt electrolytes were created by first dissolving sodium sulfate (Na₂SO₄) (≥99% anhydrous), before adding the second salt, *i.e.*, guanidine sulfate (Gua₂SO₄) (99%), magnesium acetate tetrahydrate (MgAc₂) (ACS reagent, ≥98%), or magnesium sulfate (MgSO₄) (≥99.5% anhydrous). All salts were bought from Sigma-Aldrich.

Electrode preparation usually starts with a slurry in which the materials are mixed, before being coated onto a current collector. In this thesis, commercially available working electrode (WE) active materials (PTCDA (Sigma-Aldrich), AC (Darco G-60, 600 m² g⁻¹, J.T. Baker), Fennac (Altris), NTP²) were first mixed with carbon black (Ketjenblack EC-300J), a conductive additive, with a pestle and mortar, before being added into aqueous solutions of 3 wt% carboxymethyl cellulose (CMC) (Sigma-Aldrich) binder. The slurries were then coated with a Doctor Blade on graphite foil (SGL Carbon), acting as an organic current collector. After drying in ambient air and a vacuum oven, 10 mm Ø electrodes were punched out with active material loadings ranging from 0.8-3 mg cm⁻².

3-electrode Swagelok cells (Figure 5) were assembled for both the half-cell and the full cell configurations, to enable monitoring of all electrode potentials, with Whatman cellulose filter separators (Grade 44, Sigma-Aldrich). For the former, the WEs were paired with freestanding high surface area AC counter electrodes (CEs) with several times higher active material loading.

The potential is never measured on an absolute scale, but relative to a known redox couple. For aqueous electrolytes, Ag/AgCl is a well-known and commonly used redox couple, why it was chosen as the RE (5 mm Ø, 0.127 mm silver foil, Alfa Aesar/AgCl ink, ALS Japan). The electrochemical techniques described in the coming chapters; CV, GC, and EIS, were all done with the *as described* Swagelok cell set-up, on a Biologic VMP3 multichannel potentiostat/galvanostat, except for the full cell EIS measurements which were carried out in 2-electrode coin cells (CR2032).

² NTP not commercially available, obtained from CIC energiGUNE.

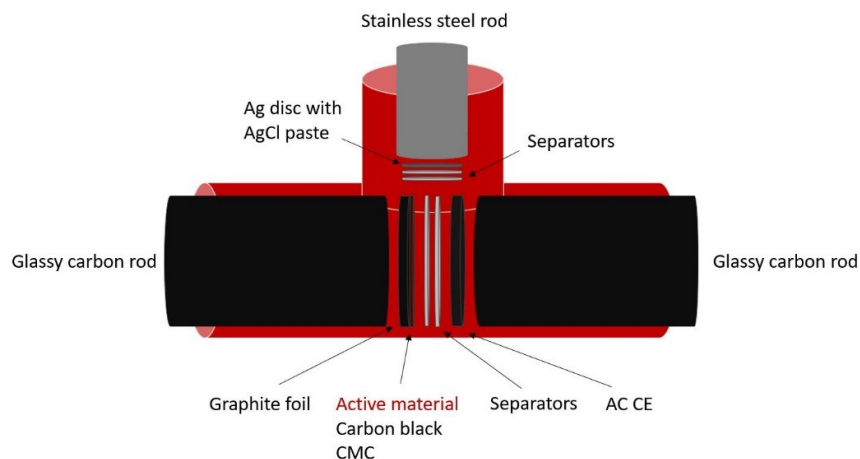


Figure 5. 3-electrode cell set-up for the electrochemical characterization of a PTCDA electrode.

LSV was done using a beaker cell (Figure 6) with a glassy carbon WE (1.2 mm Ø), a platinum (Pt) wire CE, and an Ag/AgCl (3 M NaCl) RE submerged in 2 ml electrolyte. Voltammograms were gathered using the Biologic VMP3 multichannel potentiostat/galvanostat at a scan rate of 1 mV s^{-1} and the current density limit for the ESW was set to 1 mA cm^{-2} .

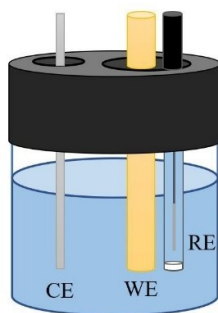


Figure 6. LSV cell set-up.

3.2 Physico-chemical characterization

3.2.1 Densitometry and viscometry

With an Anton Paar DMA 4500 M densitometer the densities (ρ) of the electrolytes were measured using the oscillating U-tube method. A U-shaped tube is set in motion by a piezoelectric actuator and depending on the mass of the electrolyte the tube is filled with; the tube resonates at different eigenfrequencies. By having a fixed volume, the densities can easily be derived. Adjacent to the densitometer, a Rolling-ball Lovis 2000 ME viscometer is coupled, working in conjunction. A glass capillary is filled with electrolyte and a metal ball is put inside before sealing. At varying angles, the capillary is tilted and the ball rolls through

the tube at varying speeds. By having a small, spherical ball with smooth surfaces, the Reynolds number will be low, resulting in laminar flow, and the drag force on the ball can be approximated by Stokes' law,

$$F_d = 6\pi r\eta v, \quad (\text{Eq. 9})$$

derived by solving the Navier-Stokes equations at the Stokes flow limit, where r is the ball radius, η is the electrolyte viscosity, and v the ball velocity. To solve for η , the gravitational force acting on the ball F_g is set to the drag force F_d , and by avoiding bubbles in the capillary, the densities and viscosities can be measured simultaneously at varying temperatures. The densities and viscosities are usually depicted in Arrhenius plots (Figure 7) where the temperature dependencies can be visualized.

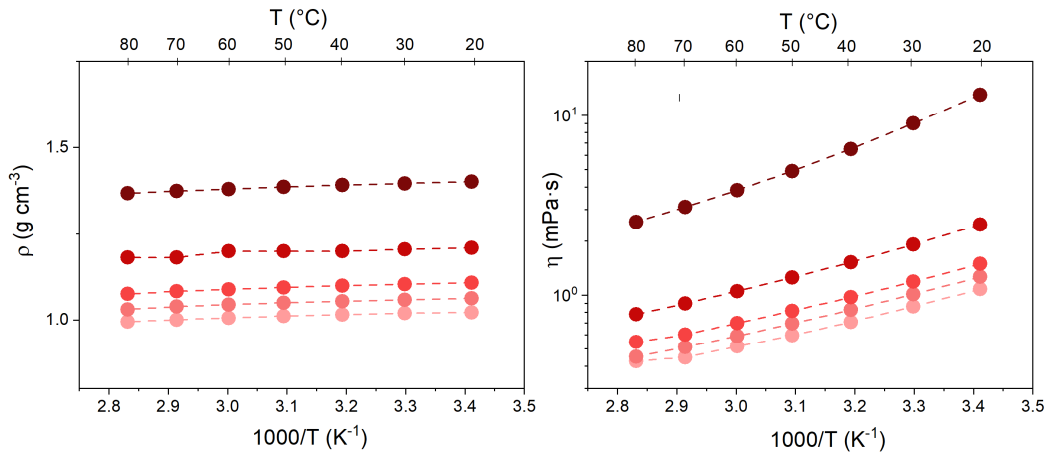


Figure 7. Arrhenius plots of the densities and viscosities of Na_2SO_4 based aqueous electrolytes. (I).

3.2.2 Ionic conductivity

The ionic conductivities (σ) were measured using a Mettler-Toledo SevenCompact S230 conductivity meter with a 12 mm InLab® 710 Cond probe with 4 Pt poles conductivity cell ($\pm 0.5\%$), temperature controlled by a home-built thermoelectric set-up. Similar to the densities and viscosities, ionic conductivities are also often visualized by Arrhenius plots (Figure 8a). The ionic conductivity of an electrolyte originates from the ionic species physically migrating in the solvent. For bulk electrolyte, diffusion – in which the movement is caused by a concentration gradient – is the main transport mechanism and the electrodes can be seen as sources/sinks of cations, where the generally higher ionic concentration close to the electrode surfaces give rise to the concentration gradient. Moreover, cations such as sodium and lithium have an affinity to water molecules, resulting in a solvation shell around the ion. This intermolecular structure is (relatively) stable and will diffuse as one large unit during transport, a so-called vehicular transport mechanism [81]. This system can be approximated by the Stokes-Einstein relation for the diffusion coefficient,

$$D = \frac{K_b T}{6\pi r\eta} \quad (\text{Eq. 10})$$

where r is the radius of the solvation shell and η the electrolyte viscosity.

The molar ionic conductivity (Λ) of the electrolyte was calculated by dividing the measured σ with the molarity (M), which in turn was derived by the measured ρ . Furthermore, the Λ was scaled to allow for a comparison to be made between the studied electrolytes and with other monovalent systems, as follows:

$$\Lambda_{eq} = \frac{1}{n^+z^+} \Lambda, \quad (Eq. 11)$$

where n^+ is the number of cations, z^+ is the charge on the cation, and Λ_{eq} is the scaled (equivalent) molar conductivity. By combining the η and the Λ of the electrolyte, an empirical rule by P. Walden concerning ions in solutions suggests that the product of the above is approximately constant for the same ions in different solvents [82],

$$\eta\Lambda = constant. \quad (Eq. 12)$$

Some justification for Walden's rule is provided by the proportional relationship between Λ and the diffusion coefficient; as D is inversely proportional to the η (Eq. 10), Λ is inversely proportional to η , which is in accordance with Walden's rule. Nevertheless, different solvents hydrate the same ions differently, this affect both the r and η when changing solvent which is a limitation of the rule. Moreover, by plotting Λ vs. η in log-log scale, a Walden plot (Figure 8b) is made and the relationship between the electrolytes' equivalent molar conductivities and viscosities can be deciphered, by qualitatively visualizing their ionicities and classifying their ion conducting behaviour. Far below the ideal KCl line are non-ionic, under the ideal line are poor-ionic, on the ideal line are good-ionic and upper left, above the KCl line, are superionic liquids or solutions [83].

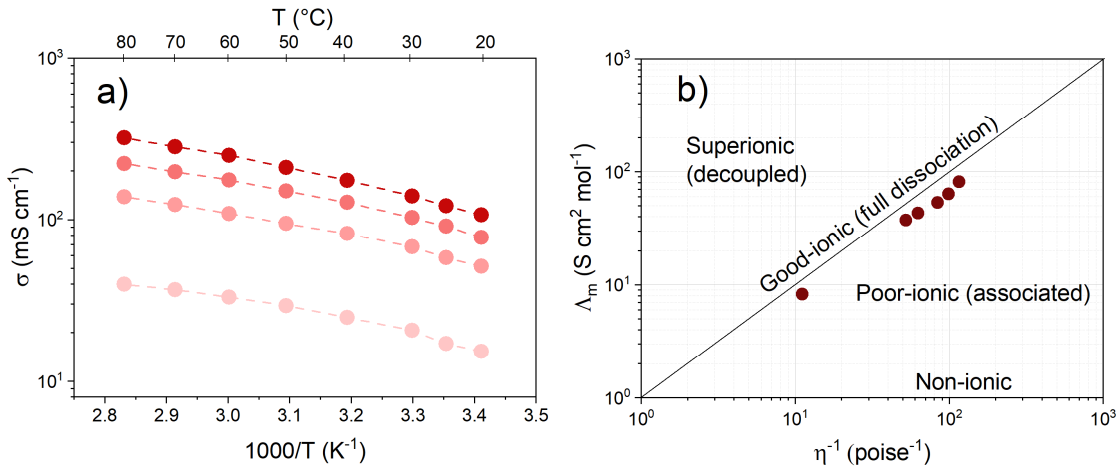


Figure 8. a) Ionic conductivity Arrhenius plot and b) a Walden plot of Na_2SO_4 based aqueous electrolytes. (I).

3.3 Spectroscopy & diffraction

3.3.1 Raman spectroscopy

Raman spectroscopy provides information about the microscopic structure and the intermolecular interactions, and it uses electromagnetic radiation to study vibrational (and rotational) transitions in molecules. These transitions appear in the $10^4 - 10^2 \text{ cm}^{-1}$ region and emerge from vibrations of the nuclei in the molecules [84]. A monochromatic laser illuminates the sample and the external electric field of the incident beam interacts with the electron cloud of a sample. A vibrational state (Figure 9) is temporarily raised to a "virtual state", energetically situated between the highest vibrational and next highest electronic state. This transition is not quantized and the inelastic scattered photons, the Raman scattering, are shifted up or down in energy (antiStokes or Stokes). This shift holds information about the vibrational modes, "structural fingerprints", of the sample which are detected by the detector. The vibrational frequencies are measured as a shift from the incident beam frequency and are correlated to certain molecules.

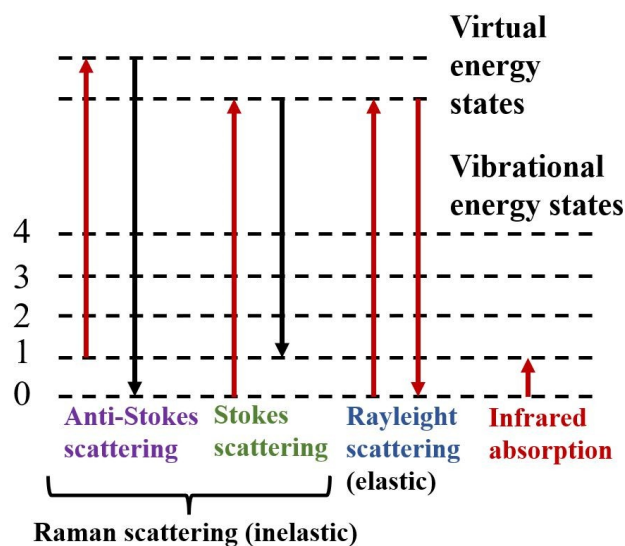


Figure 9. Energy level diagram of the states involved in Raman spectroscopy.

Raman spectroscopy is a useful technique to study the local water structure of aqueous electrolytes, and by investigating the OH-stretching vibrations ($2800-4000 \text{ cm}^{-1}$) the relative amount of free water in the electrolyte can be determined. By spectral fitting and peak deconvolution, the spectra can be broken down and analyzed, as the contributions of different OH vibrations are distinguished. Authors differ in how many peaks they assign, typically varying from two to five Gaussians, and Sun assigned five bands: 3005 cm^{-1} , 3226 cm^{-1} , 3434 cm^{-1} , 3573 cm^{-1} and 3640 cm^{-1} to O-H vibrations engaged in DAA, DDAA, DA, and DDA hydrogen-bonding, and free O-H vibrations, where D stand for a proton donor and A refer to a proton acceptor [85]. The analysis is typically done by comparing the intensities and areas of the DA-OH and DDAA-OH peak, and increased ratios indicates a decreased amount of free water in the electrolyte.

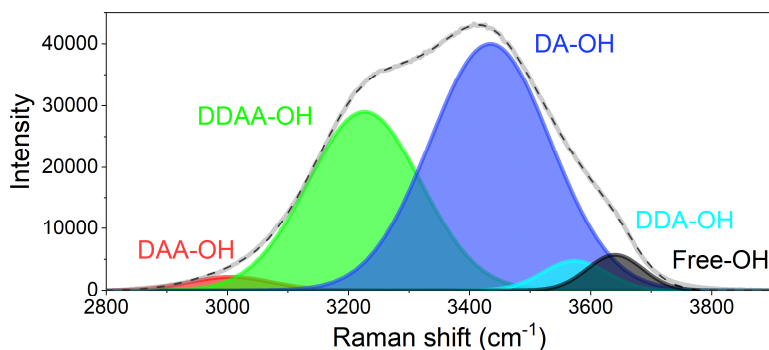


Figure 10. Raman spectra in the O-H stretching vibration region and the corresponding peak deconvolution of pure water [85]. (I).

3.3.2 Fourier-transform infrared spectroscopy

Infrared spectroscopy (IR) uses infrared electromagnetic radiation to measure the interaction with matter by absorption, emission or reflection, and it is used to study and identify compounds or functional groups in solids, liquids, or gases. As molecules above 0 K are non-stationary, they vibrate and absorb frequencies characteristic of their structure. For the sample to be IR active, the vibrational modes need to be associated with a dipole moment change. A common sampling technique used with IR is attenuated total reflection (ATR), where an evanescent wave arises from an infrared beam having total internal reflection in the ATR crystal. The sample is situated next to the crystal, in this case a germanium crystal due to its high refractive index, and absorbs light which is later registered in the detector.

Herein, a Bruker Alpha ATR Fourier-transform IR (FTIR) spectrometer was used, where all the infrared frequencies are measured simultaneously, enabling fast measurements. By introducing an interferometer with a beam splitter, the infrared beam is split into two, and in short, they are reflected by mirrors, interact with each other, and when returning to the beam splitter they have traveled different distances. The resulting interferogram is then Fourier transformed into an IR spectrum. FTIR spectroscopy was used to study the functional groups of the PTCDA powder and the PTCDA electrodes.

3.3.3 Powder X-ray diffraction

X-rays are electromagnetic radiation with a characteristic wavelength (λ) in the Ångström range ($1 \text{ \AA} = 10^{-10} \text{ m}$). Photons of such high frequency is commonly used to characterize the crystal structure(s) of compounds by the diffraction phenomena, hence X-ray diffraction (XRD). A Bruker D8 Discover set-up with Cu radiation was used in a Bragg-Brentano geometry with a Ni filter to cut Cu K- β contributions. By directing the beam towards the sample in different angles (θ), constructive interference is produced when Bragg's law is satisfied, according to

$$n\lambda = 2d\sin\theta, \quad (\text{Eq. 13})$$

where n is a positive and d relates to the lattice spacing in the crystal structure. The resulting diffractogram generates peaks on the 2θ x-axis with corresponding intensities, and the peak's

positions can be seen as “fingerprints”. By identifying each peak, the crystal phases present in the sample can be determined. This technique was used *ex situ* to characterize the prepared PTCDA electrodes in different state-of-charge, to study if, and how, the lattice parameters were changed during cycling, as Na^+ had been intercalated or deintercalated into the crystal structure.

3.4 Electrochemical characterization

3.4.1 Linear sweep voltammetry

The electrochemical stability of an electrolyte is important to be aware of, to know the voltage range the battery can operate in, and when unwanted side reactions or water splitting of the aqueous electrolyte occurs. LSV was used to measure the ESW of the electrolytes; by applying a constant voltage rate, the responding current is measured, and a current density limit is set to define ESW (Figure 11). At this point the current from the chemical reactions are no longer negligible and for absolute potentials higher than this, the electrolyte is no longer stable. Although, defining the stability of an electrolyte and comparing ESWs is not straight forward. To begin with, the current density limit is not set in stone, varying vastly among authors, and is sometimes not communicated. Similarly, the scan rate varies, which influences the current response and induces overpotentials. Moreover, the temperature and electrolyte volume – rarely discussed – need to be similar for a fair comparison to be made. Finally, the WE and CE have a big influence on the onset of OER/HER as the *materials* can have overpotentials, moving the water splitting reaction to higher voltages [86].

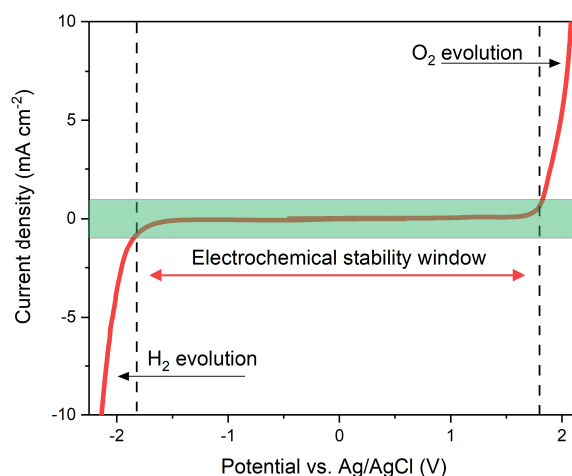


Figure 11. Voltammogram with the green region and dashed lines outlining the ESW.

3.4.2 Cyclic voltammetry

Similar to LSV, cyclic voltammetry (CV) sweeps the set potential range of the WE and records the current response. The resulting voltammogram shows the electrochemical behavior of the material and holds information about the charge storage mechanisms. By

analyzing the voltammogram, it is possible to determine at what potentials the redox reactions occur, what kind of reactions occur, and in what magnitude the reactions occur. This was a crucial tool in the initial stages for all active materials, as quick scans were made to figure out if material's redox activity, before more elaborate electrochemical investigations.

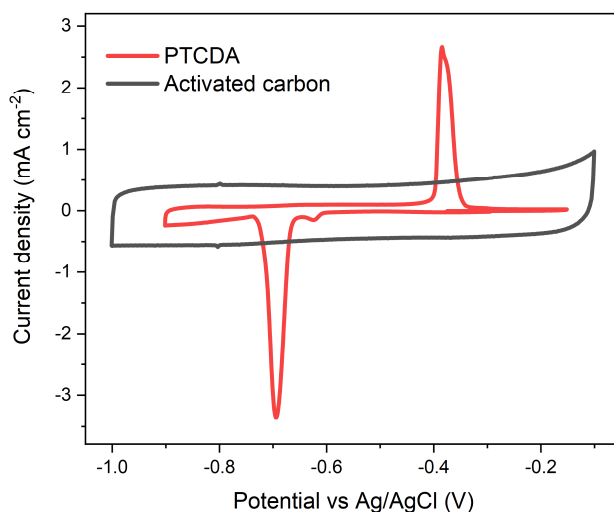


Figure 12. Cyclic voltammogram.

The characteristic Faradaic and non-Faradaic behavior are illustrated for PTCDA and AC (Figure 12) where the former displays distinct redox peaks at specific potentials, while the latter has rectangularly shaped profiles throughout the entire voltammogram. This is due to the different charge storage mechanisms, where, the peaks originate from an electron flow from an oxidation or reduction reaction [87], while the rectangular shapes originate from the continuously forming charged double layer at the electrode surface.

In CV, the scan speed is chosen depending on what material and what mechanism is studied. Slower speeds ($<0.5 \text{ mV s}^{-1}$) are often applied when characterizing redox active materials, and especially new materials, as the peaks will be sharper and more easily interpreted. Faster speeds ($> 10 \text{ mV s}^{-1}$) are applied for supercapacitor materials, or when the actual behavior and performance of the system is to be analyzed. Only higher scan rates may test if the charge storage mechanism is fast, if the peaks will remain sharp and with small separation, important for high power applications. In this work a variety of scan speeds have been utilized, ranging from 0.2 mV s^{-1} up to 50 mV s^{-1} , depending on what material and what mechanism was of interest.

3.4.3 Galvanostatic cycling

The most widely used electrochemical test for batteries and hybrid supercapacitors is galvanostatic cycling (GC), as this is similar to how charge storage devices operate. During GC, a constant current is applied, and the resulting voltage is recorded, creating charge/discharge curves (Figure 13), where the capacity of the electrode (or cell) can be measured ($I \cdot t$). Faradaic materials show flat plateaus corresponding to the redox reactions happening, whereas non-Faradaic materials instead have sloping profiles with linearly

increasing capacity. GC can also be used to calculate the energy/power densities, popular performance measures even outside the battery field, enabling comparisons between different energy storage technologies.

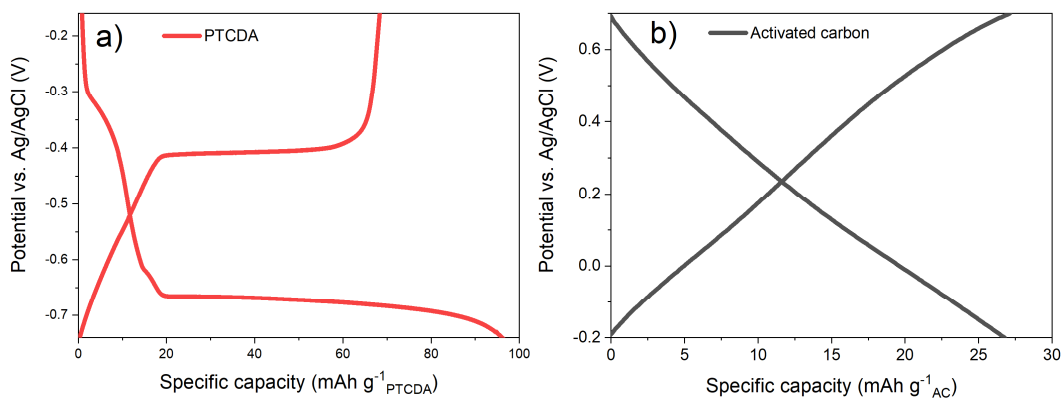


Figure 13. GC charge/discharge curves.

3-electrode configurations are common when studying electrodes in half-cells, by also doing this when cycling full cells, all electrode potentials can be monitored simultaneously (Figure 14a). This is important for understanding the electrochemical behavior of the separate electrodes, and furthermore, particularly useful when weight balancing cells. By running the Na-HSCs in 3-electrode Swagelok cells, the charge/discharge profiles were monitored, and *e.g.*, if the capacity (and thereby weight) of the AC electrode was not sufficiently high, this would instantaneously be illuminated as the voltage plateau of the PTCDA electrode would not be fully utilized. Well-balanced cells make use of the entirety of the plateau (Figure 14) and deliver full cell capacities similar to the stand-alone working electrode capacity.

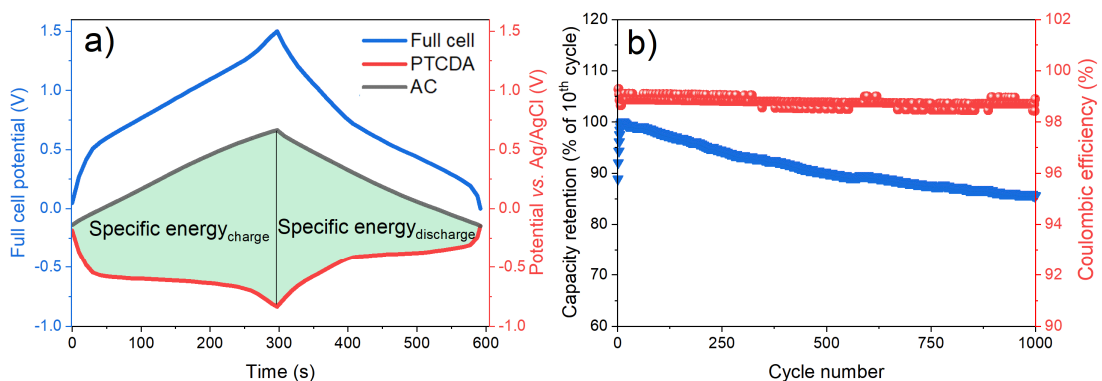


Figure 14. a) GC charge/discharge curves and b) cycling stability test of a PTCDA//AC full cell. (II).

A final way to use GC is to study the cycling stability (Figure 14b). This is done by doing many galvanostatic cycles and recording the capacity at each cycle. The capacity retention can thus be calculated as the ratio of the remaining capacity and the initial capacity ($Q_{final}/Q_{initial}$). The corresponding Coulombic efficiency for each cycle, i.e., $Q_{discharge}/Q_{charge}$ is another measure used to provide information how much useful capacity, in percent, that can be withdrawn, or in other words, how much capacity is lost at each cycle. Last but not

least, the energy efficiency of an electrode, or a full cell, can be extracted as the area ratio between the specific energy of discharge vs. charge ($E_{discharge}/E_{charge}$), extracted from the areas between the charge/discharge curves (Figure 14a).

3.4.4 Electrochemical impedance spectroscopy

Finally, EIS was used as a tool to study the resistances in the assembled cells, both in 2-electrode and 3-electrode configurations. A sinusoidal voltage perturbation of ~ 5 mV is usually applied, and the phase and the magnitude of the current is recorded. The applied voltage must be small not to induce charging or discharging, and so the current responds linearly to the voltage. By doing this in a frequency sweep (e.g. 100 kHz – 100 mHz) a Nyquist plot (Figure 15) is created with the complex cell impedance $Z(f)$ as a function of frequency.

Choosing circuit models is not straight forward, but by implementing the simple and commonly used Randles circuit cell model, physical properties such as the charge-transfer resistance (R_{ct}) and the electrolyte resistance (R_s) can be extracted from the Nyquist plot, where C_{dl} and Z_w represent the double layer capacitance and the Warburg diffusion element, respectively. This was done for the stand-alone electrodes in Swagelok cells, but to ensure more reproducible and comparable results, the full cells were studied in 2-electrode coin cells where the applied pressure between the two electrodes was kept more constant.

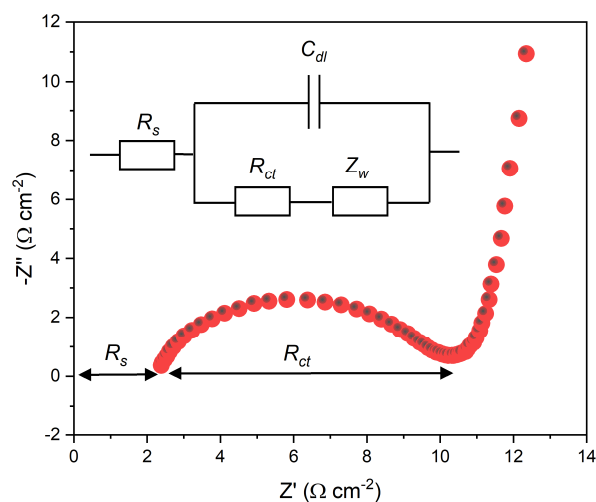


Figure 15. Nyquist plot and Randles circuit.

4. Results & Discussion

4.1 Developing the hybrid electrolyte

Starting from the standard and most commonly used aqueous Na-ion ESD electrolyte 1 M $\text{Na}_2\text{SO}_{4(\text{aq})}$, the idea was to find suitable additives which would enhance the ESW. This was an unexplored path which had (and have) a lot of potential as the stock solution of saturated (*ca.* 1.9-2.0 m) Na_2SO_4 has a very low viscosity (*ca.* 1.9 mPa·s) and high ionic conductivity (*ca.* 140 mS cm^{-1}) at 30°C. Thus, introducing additional components, which in most cases increases the viscosity and decreases the ionic conductivity, will most likely not be detrimental for the battery performance as 20 times the viscosity or one-hundredth of the ionic conductivity would be sufficient for practical use. The restrictions were not to incorporate compounds that would drastically affect the cost, safety, or sustainability of the electrolyte.

4.1.1 Guanidine salt

The guanidinium cation ($\text{C}(\text{NH}_2)_3^+$ or $[\text{Gua}]^+$) is known to denature proteins by interacting with the water molecules [88], and the hypothesis was that the ESW could be broadened by binding free water with a guanidine salt. Gua_2SO_4 was chosen to not introduce more than one component at once, and at first it seemed promising due to its high solubility in water. Even in saturated Na_2SO_4 the salt dissolves up to 9.0-10.0 m, creating a WIBE. When recording LSV curves at 1 mV s^{-1} and setting the current limit to 1 mA cm^{-2} , the ESW expands slightly after adding the second salt, about 40 mV. This likely lay within the error bars, but a notable change happens during oxidation. Here, the profiles are similar, but offset (Figure 16b), why changes in the kinetics (viscosity) might be the route cause, affecting the water diffusion and therefore the onset of gas evolution.

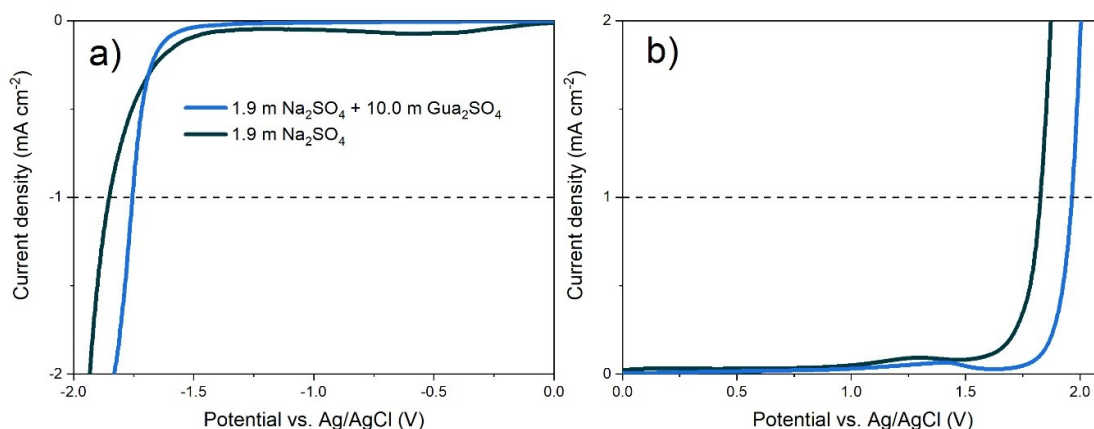


Figure 16. ESW of the aqueous electrolytes measured by LSV. A zoom-in of a) the reduction and b) the oxidation. Dashed lines at $\pm 1 \text{ mA cm}^{-2}$ to mark the stability limit.

Raman spectroscopy was thereafter applied to analyze the OH-stretching modes of water molecules, situated at 2800-4000 cm^{-1} , to provide insight on the local structure. From the Raman spectrum (Figure 17a) the $[\text{Gua}]^+$ seemed to interact with the SO_4^{2-} , instead of interacting with free water, as the ν_1 vibrational modes of SO_4^{2-} (*ca.* 982 cm^{-1} [89]) and $[\text{Gua}]^+$

(ca. 1012-1015 cm^{-1} [90]) were shifted up and down, respectively. The overall intensity of the OH-stretching vibrations *does* decrease when adding the guanidine salt, but after deconvolution, the peak intensity and area ratios (I_{ratio} and A_{ratio} , respectively) of the 3434 cm^{-1} and 3226 cm^{-1} are not increasing (Table 2), thus not indicating a decrease of free water molecules. This WIBE was therefore disregarded and not analyzed further.

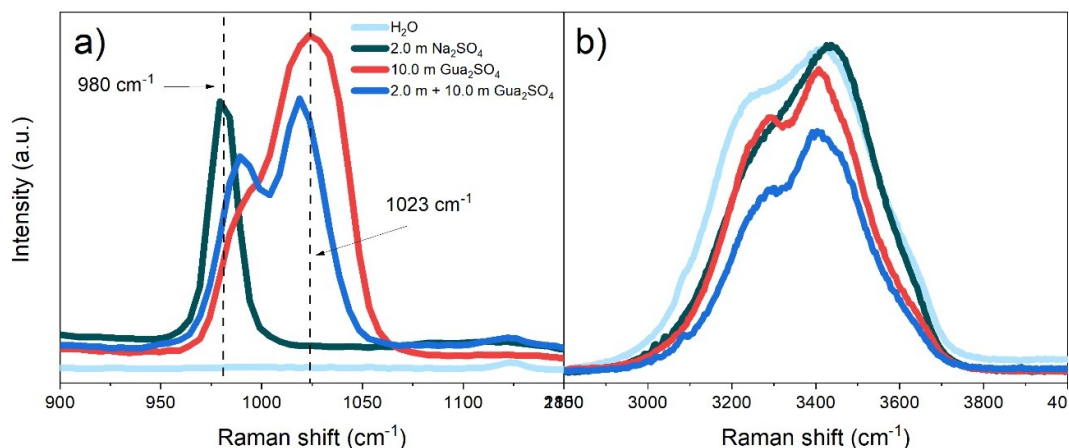


Figure 17. Raman spectra of Na_2SO_4 and Gua_2SO_4 based aqueous electrolytes.

4.1.2 Magnesium and calcium salts

The search for electrolyte additives continued, and the abundant elements Mg and Ca were considered. Several salts meeting the requirements were found and mixed with saturated Na_2SO_4 . The Ca salts (CaAc_2 and CaSO_4) unfortunately has extremely low solubilities, while MgAc_2 and MgSO_4 dissolves much easier. For the former Mg salt, when applying LSV, the acetate ion is being oxidized before the OER (Figure 18), instead narrowing the ESW. The highest concentration (2.0 m Na_2SO_4 + 1.0 m MgAc_2) also had troubles measuring Raman as it did not completely dissolve, and it was therefore disregarded as well.

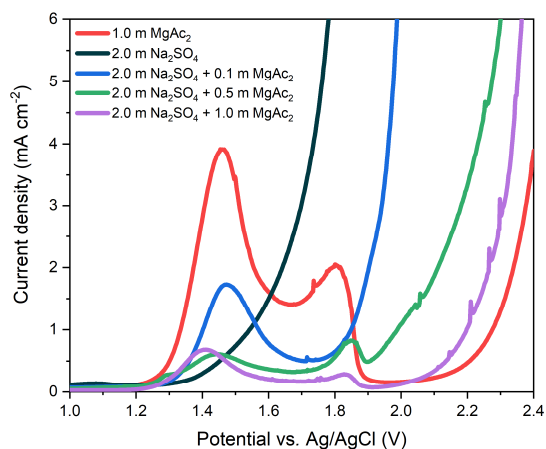


Figure 18. LSV of aqueous electrolytes based on Na_2SO_4 and MgAc_2 .

MgSO₄ on the other hand not only dissolves more than twice the amount compared to MgAc₂, the newly made “hybrid electrolyte” which consists of 1.9 m Na₂SO₄ + 2.4 m MgSO₄ also shows promising results when applying LSV (Figure 19).

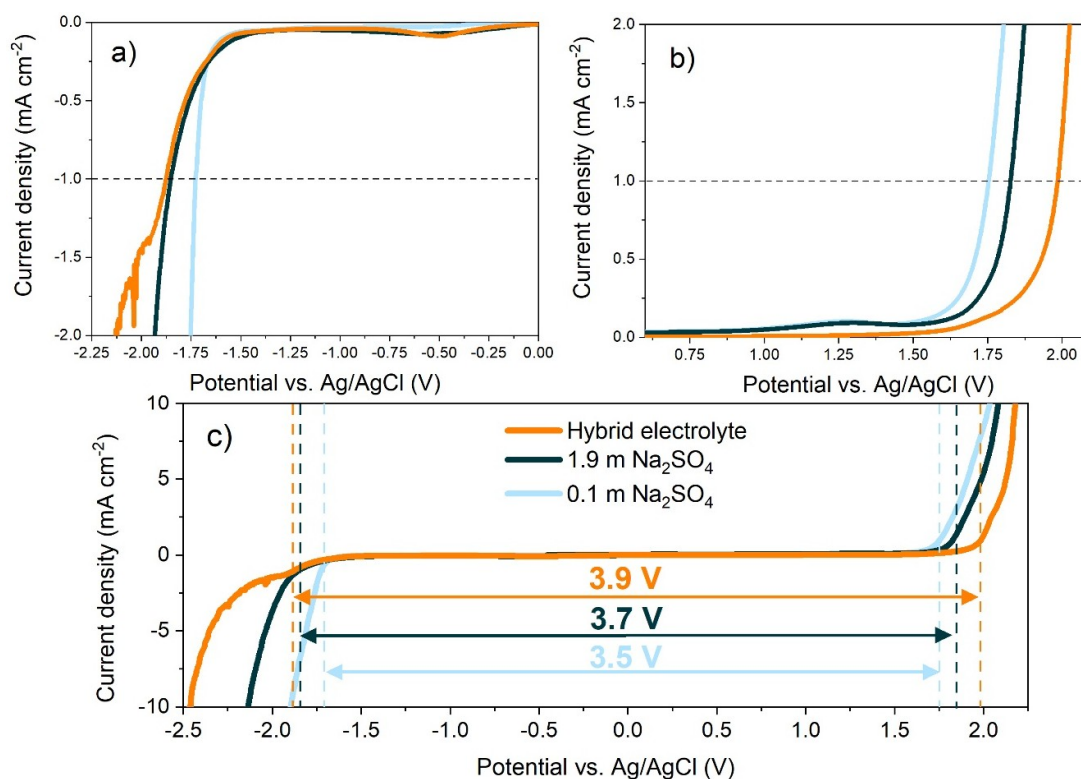


Figure 19. ESW of the aqueous electrolytes measured by LSV. A zoom-in of a) the reduction and b) the oxidation and c) a depiction of the full window. Dashed lines at $\pm 1 \text{ mA cm}^{-2}$ to mark the stability limit. (I).

The ESW expands from 3.5 V to 3.7 V (Figure 19c) by increasing the salt concentration from 0.1 m to 1.9 m, using the same scan rate and current density limit as above. ESWs for 1 M Na₂SO₄ have been reported from: 1.5-2 V on stainless steel at 0.1 mV/s to 2.2 V using Ti grids at 5 mV/s [91,92]. Compared to the literature our 1.9 m electrolyte ESW is large, but finding comparable data is difficult, as discussed in Section 3.4.1. The hybrid electrolyte results in an even wider ESW of 3.9 V, and the wave like current density increase at *ca.* 1.25 V during the oxidation (Figure 19b) is completely suppressed in the hybrid electrolyte, thus showing a considerable stability increase. The viscosity most likely has an affect here as well.

From the LSV it is clear that there is some kind of substantial difference in the ESWs. Again, Raman spectroscopy was therefore applied to analyze the OH-stretching modes of water. A shift and a sharpening of the overall broad band envelope is seen as function of salt concentration, including the hybrid electrolyte (Figure 20a).

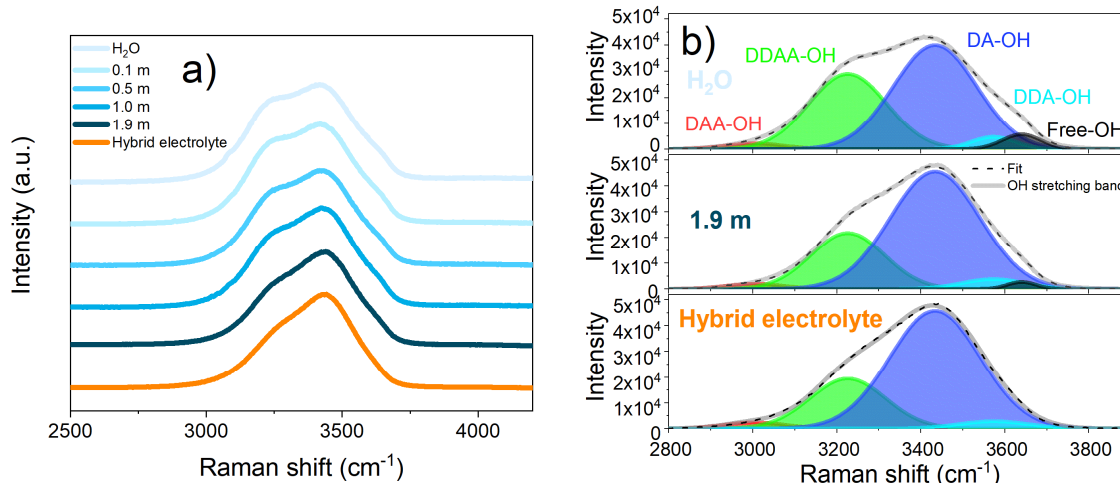


Figure 20. a) Raman spectra in the O-H stretching vibration region and b) the corresponding peak deconvolution of the pure water, the 1.9 m Na_2SO_4 electrolyte, and the hybrid electrolyte. (I).

The Raman spectra of pure H_2O , 1.9 m Na_2SO_4 , and the hybrid electrolyte were further deconvoluted into Gaussians (Figure 20b). A comparison of the I_{ratio} and A_{ratio} of the 3434 cm^{-1} and 3226 cm^{-1} bands clearly reveal the ratios increase with increasing salt concentration (Table 2), indicating the hydrogen bonded “free” water contribution relatively decreases [85,93]. By their very compositions, the 1.9 m Na_2SO_4 and the hybrid electrolytes have $\text{H}_2\text{O}/\text{cation}$ ratios of 14.6 and 9.0, respectively, and as the Walden plot (Figure 22) indicates similar ionicities, the latter electrolyte should have less “free” water available. We therefore attribute the wider ESW to a combination of higher viscosity and a decreased amount of free water. Yet, we are far from seeing the same narrow $\sim 3550 \text{ cm}^{-1}$ peak that emerges for WISEs/WIBEs at very high salt concentrations ($>20 \text{ m}$) and correspond to $\text{H}_2\text{O}/\text{Na}^+$ ratios of 2-3 [94].

Table 2. Intensity and peak area ratio of the deconvoluted peaks at 3434 cm^{-1} and 3226 cm^{-1} as well as the total OH-band area between $2800\text{-}4000 \text{ cm}^{-1}$, and the corresponding water concentration.

	I_{ratio}	A_{ratio}	A_{tot}	$C_{\text{water}} \text{ (M)}$
H_2O	1.38	1.47	1.84460E7	55.51
1.9 m	2.09	2.55	1.83039E7	52.27
1.9 + 2.4 m*	2.35	2.81	1.78139E7	49.73
2.0 + 10 m**	2.02	2.36	5.85786E6	-

* MgSO_4 . ** Gua_2SO_4 .

To further characterize the promising hybrid electrolyte, the effect of salt concentration on the physico-chemical properties; ionic conductivity, viscosity, and density were studied for temperatures up to $80 \text{ }^\circ\text{C}$. The densities of the electrolytes increase more or less linearly as a function of salt concentration (Figure 21a), while the viscosities increase exponentially (Figure 21b), and as expected both decrease as a function of temperature (Figure 21ab). The

hybrid electrolyte displays a viscosity of *ca.* 9 mPa·s at 30°C, which is half an order of magnitude higher than for the most concentrated Na₂SO₄ based electrolyte (*ca.* 1.9 mPa·s at 30°C) but compared to WISEs, the hybrid electrolyte is still very fluid; *e.g.* a 35 m NaFSI WISE renders 97 mPa·s [95].

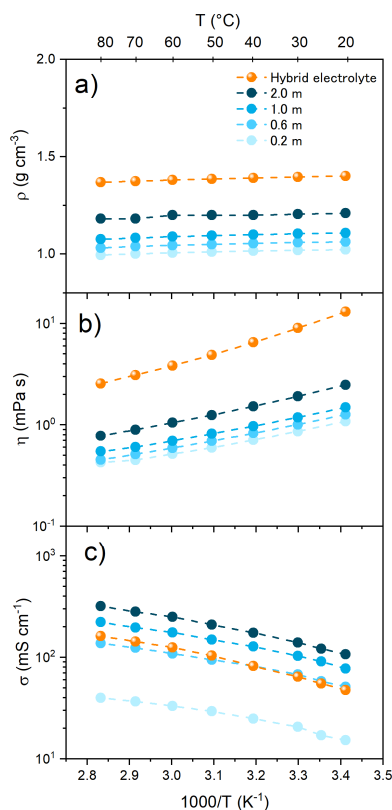


Figure 21. Arrhenius plots of the: a) density, b) viscosity, and c) ionic conductivity for the Na₂SO₄-based aqueous electrolytes. Dashed lines to guide the eye only. (I).

The intrinsic high ionic conductivities of aqueous electrolytes are also witnessed here (Figure 21c), and in the same order of magnitude as NaTFSI, NaFSI and NaClO₄ based aqueous electrolytes [96]. Moreover, the ionic conductivity for the hybrid electrolyte decreases less than what would be expected based on the increased viscosity, relative to the same Na₂SO₄ concentration, to 55 mS·cm⁻¹ at 30°C, pointing to some synergy. There is clearly an increase in the charge carrier concentration, but perhaps also somewhat different structure and dynamics as the temperature dependence differs (Figure 21c).

Finally, a Walden plot is made to study the relationship between the electrolytes' equivalent molar conductivities and viscosities [82], and qualitatively visualize their ionicities. The Na₂SO₄ based electrolytes, including the hybrid electrolyte, are all close to the ideal KCl line and thus the salts fully dissociate when immersed in water (Figure 22). Furthermore, as the slopes are close to unity, the activation energies for ionic conductivity and viscosity are similar, and hence the ion transport mechanism is very likely to be mainly vehicular [97].

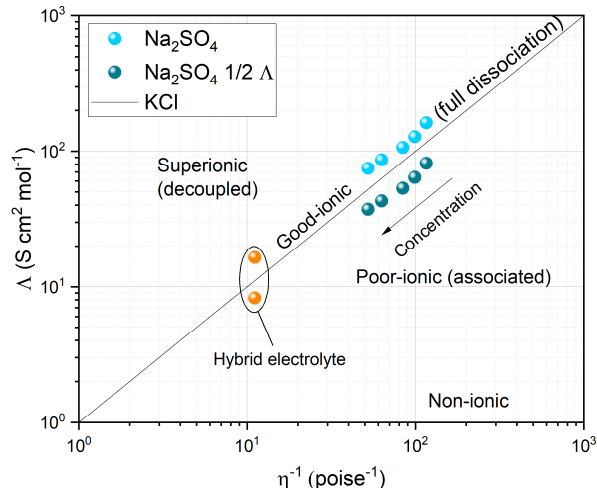


Figure 22. Walden plot of the aqueous electrolytes at 30°C. The $\text{Na}_2\text{SO}_4 \frac{1}{2} \Lambda$ data are using scaled molar conductivities (see text). (I).

The divalent Mg^{2+} makes comparisons with monovalent systems more intricate, and how to properly represent the data in a Walden plot is not trivial. Dave *et al.* compared aqueous Na_2SO_4 and NaNO_3 electrolytes and argued the (apparent) higher ionicity of the former to originate from the stoichiometry difference [98]. Moreover, the highly charged SO_4^{2-} could also make less solvent available for the cation, rendering smaller Na^+ first solvation shells. Unlike Dave *et al.*, we instead apply a scaling methodology and divide the molar conductivities by two ($\text{Na}_2\text{SO}_4 \frac{1}{2} \Lambda$), according to Equation . 11. Then, the ionicities of our electrolytes become akin to aqueous NaTFSI and NaFSI electrolytes [99]. On the other hand, considering the measured molar conductivities, all the electrolytes can be classified as slightly superionic, *i.e.* the ionic conductivity and the viscosity are somewhat decoupled, thus the ions move faster than expected solely based on the viscosity [100]. Worth noting is the hybrid electrolyte data are positioned furthest away from the ideal line and thus display the highest ionicities.

4.1.3 Prospective additives

Going forward, with the intention to further develop the hybrid electrolyte, additional additives need not be limited to salts. Indeed, two new additive concepts were recently demonstrated, where, first, hydrophilic mono/disaccharides were used to create “water-in-sugar” electrolytes [101]. Improved cycling stabilities and extended ESWs were achieved as a result of a formed glucose film on the electrode surface and a decreased amount of free water molecules, destroying the tetrahedral structure of water, thus lowering the binding degree of water molecules via the break of hydrogen bonds. Second, surfactants have been applied to electrolytes as well, with similar results as the water-in-sugar electrolytes, since their chemistry allow them to form a monolayer of molecules on the electrode surfaces [102].

If possible, creating an electrolyte composed of several salts, sugars, and possibly also surfactants, could have synergistic effects to increase the ESW of $\text{Na}_2\text{SO}_4(\text{aq})$ and decrease active material dissolution. The latter is the topic of next section.

4.2 Suppressing the dissolution of active materials

A considerable drawback of aqueous electrolytes is the high solubility of many active electrode materials. Herein, we investigate if the hybrid electrolyte can improve the electrochemical performance of different electrodes by suppressing active material dissolution, compared to 1 M Na₂SO_{4(aq)}. Furthermore, sustainable electrodes of commonly used ASIB/Na-HSC active materials (Na-based PBA, NTP, and AC), as well as PTCDA, were made with organic binders (CMC), separators (cellulose filter paper), and current collectors (graphite foil).

4.2.1 Fennac

First out, the commercial PBA Fennac (Na_xFe[Fe(CN)₆]·yH₂O) was investigated by CV and GC. The rate capability tests with GC (and Pt) CEs resulted in bad rate retentions (Figure 23a), as the low surface area turned out to be a bottle neck for higher currents. Therefore, AC CEs with several times higher active material loading were used hereafter, indeed improving the rate capability significantly (Figure 23b).

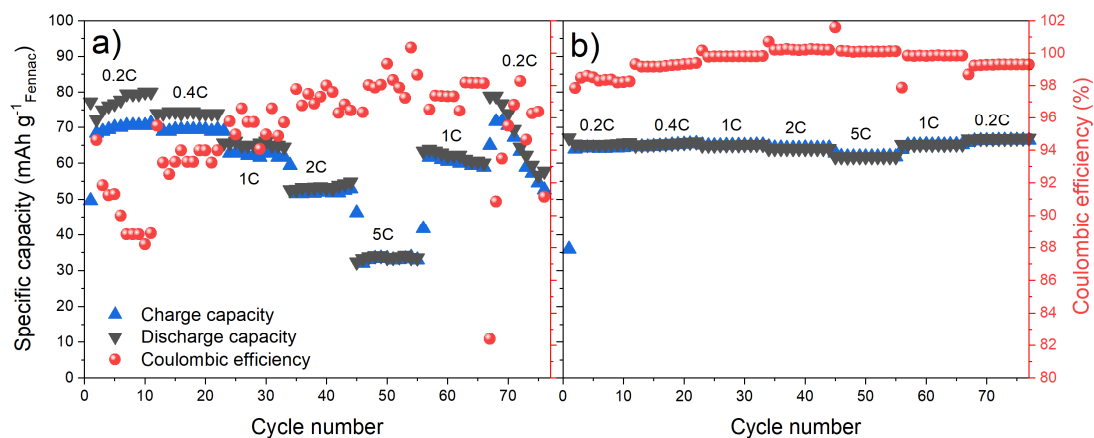


Figure 23. Rate capability test of Fennac electrodes with a) GC CE and b) AC CE, with the hybrid electrolyte between 0.4 and -0.3 V vs. Ag/AgCl.

Voltammograms were recorded at varying sweep rates, and during oxidation at 0.2 mV s⁻¹ with 1 m Na₂SO_{4(aq)}, Fennac has a predominant redox peak at ca. 0.1 V vs. Ag/AgCl and a minor peak ca. 0.09 V higher, denoted together as the 1st redox peak (inset Figure 24). During reduction the peak is broader, starting at ca. 0.025 V, without a clear “end”. In contrast, Fennac displays two adjacent redox peaks at ca. -0.03 V and 0.1 V vs. Ag/AgCl during oxidation with the hybrid electrolyte, and slightly down shifted during reduction (inset Figure 24b). The current density is more than ten times higher, and the voltage profiles are significantly more symmetric with the hybrid electrolyte, suggesting improved electrochemical behavior. This difference is most likely due to co-intercalation of Na⁺ and Mg⁺ as PBAs have shown to reversibility intercalate Mg⁺ [103]. In comparison, Fennac behave similarly with 1.0 m as with saturated Na₂SO_{4(aq)}, only differing with a slight shift and a more evenly split 1st peak during oxidation (inset Figure 24a).

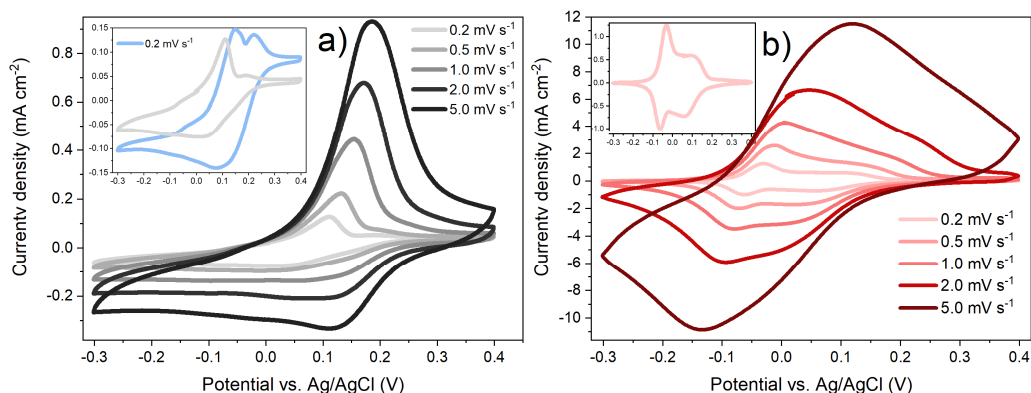


Figure 24. Voltammogram of Fennac electrodes with the a) 1 m $\text{Na}_2\text{SO}_{4(\text{aq})}$ and b) hybrid electrolytes. Inset in a) also includes 1.9 m $\text{Na}_2\text{SO}_{4(\text{aq})}$ (blue).

The GC charge/discharge curves and rate tests of Fennac with 1.0 m $\text{Na}_2\text{SO}_{4(\text{aq})}$, 1.9 m $\text{Na}_2\text{SO}_{4(\text{aq})}$, and the hybrid electrolytes differ to a large extent. The former fails to deliver a stable and reversible capacity (Figure 25ad), whereas with 1.9 m $\text{Na}_2\text{SO}_{4(\text{aq})}$ Fennac displays higher stability and reversibility (Figure 25b), with capacities similar to other Na-based PBAs [48,49]. At 0.2C however, Fennac fail to cycle with both electrolytes (inset Figure 25ab). In stark contrast, Fennac with the hybrid electrolyte exhibit excellent cycling stability, Coulombic efficiency, and capacity retention throughout all scan rates (Figure 25cf). In addition to Mg^+ co-intercalation, a peptization process [49], resulting in colloidal active material particles could be the cause of the difference, where the reaction is mitigated in the hybrid electrolyte. The reaction is thought to be due to a repulsive effect from the positive charge on the electrode surface and O_2 bubbling from the OER resulting in O_2 adsorption on the PBA particles [49]. The higher viscosity and higher electrolyte stability of the hybrid electrolyte could, in theory, suppress this reaction, but the separators were not recovered post cycling, which would have confirmed the presence or absence of blue particles.

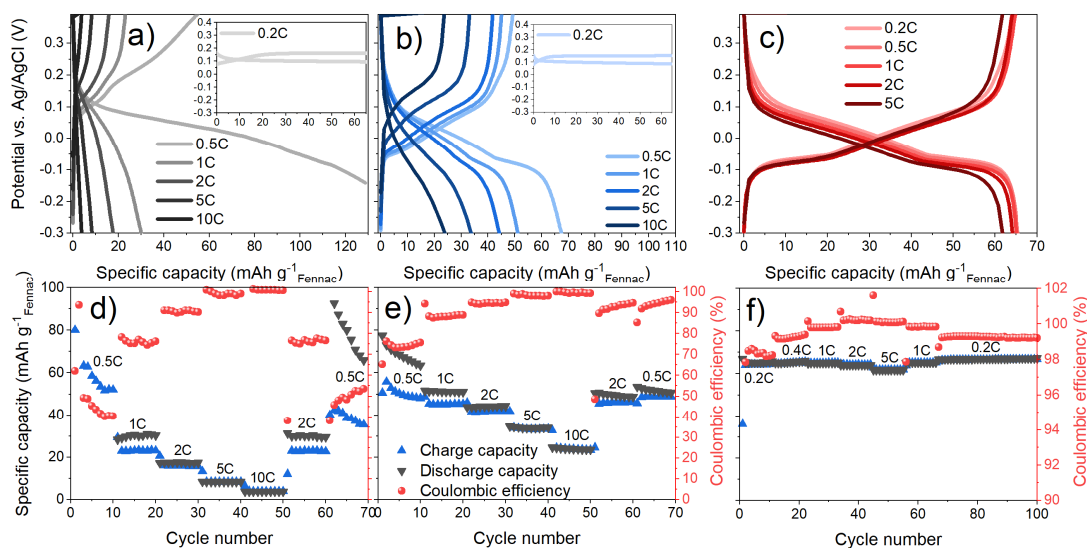


Figure 25. Fennac electrode a-c) GC and d-f) rate capability test with a, d) 1.0 m $\text{Na}_2\text{SO}_{4(\text{aq})}$, b, e) 1.9 m $\text{Na}_2\text{SO}_{4(\text{aq})}$, and c, f) the hybrid electrolytes.

A 2nd peak can be found at much higher potentials, *ca.* 1.1 V during oxidation and *ca.* 0.7 V vs. Ag/AgCl during reduction (Figure 26) when recording the voltammogram at 5 mV s⁻¹. Utilizing this peak is, however, problematic as current from the OER becomes significant at potentials >1.15-1.2 V.

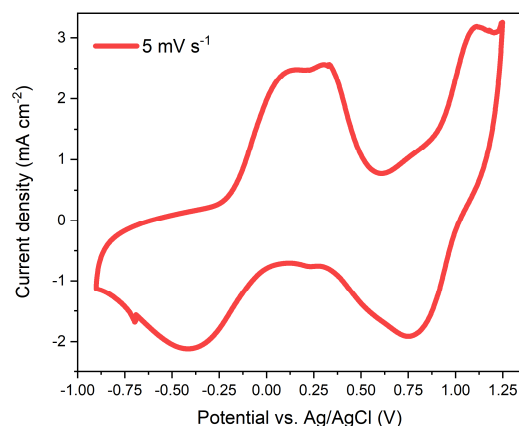


Figure 26. Voltammogram of a Fennac electrode with the hybrid electrolyte.

Yet, the 2nd peak can be used if the cut off voltage and scan rate is tuned. By cutting the voltage before any substantial OER, a high capacity of *ca.* 84 mAh g⁻¹ (1C) and an agreeable Coulombic efficiency is obtained (1C-5C Figure 27ab), unlike for the lower C-rates (0.2C-0.5C Figure 27ab). Still, the voltage cannot be cut too low, especially not for very high C-rates with induced overpotentials, as the redox plateau then will not be reached, resulting in a suffered capacity (10C-50C Figure 27cd).

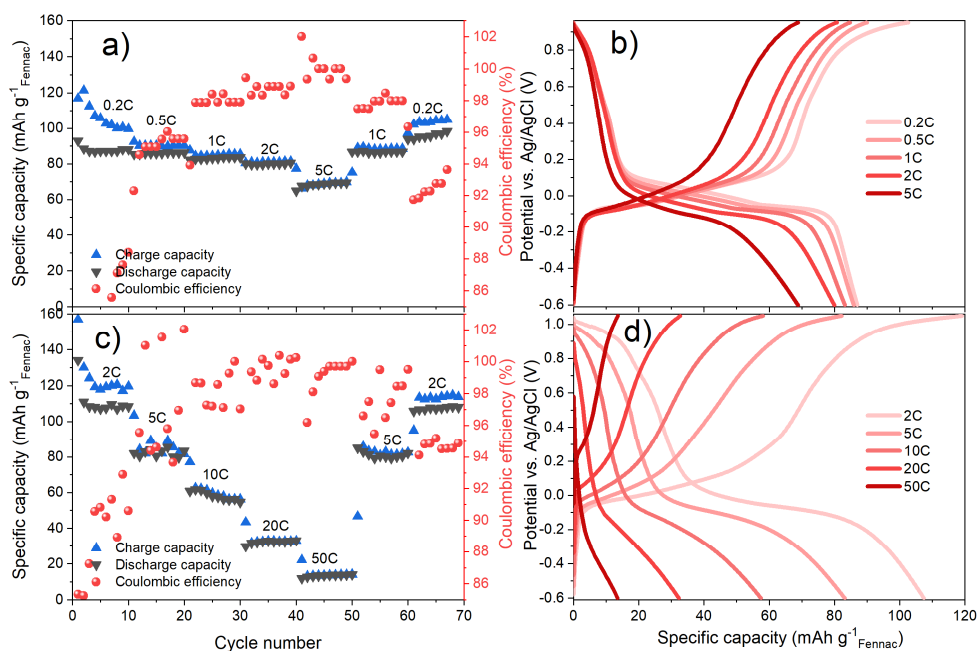


Figure 27. Fennac electrode a,c) rate capability and b,d) GC with the hybrid electrolyte.

Fennac clearly is a viable active material with the hybrid electrolyte using the 1st peak. However, the 2nd peak is tricky in three parts; the cut off voltage needs to be tuned for high Coulombic efficiencies, as the weight balancing of the anode/cathode affects how much of the redox plateau is utilized. Second, the cut off voltage – tuned for a certain weight ratio – only holds true for small deviations in the applied current, limiting the device from versatile use in terms of charging and discharging rates. Third, the voltage difference between the 1st and the 2nd plateau is almost 1 V. In practice, the device delivers *ca.* half the capacity at differential potentials from *x* V to *x*-1 V, and the remaining half at *ca.* *x*-1 V. With NTP as anode this is *ca.* 1.9-0.9 V and *ca.* 0.9 V, which could be hard to find applications for.

4.2.2 NTP

The anode material NTP was studied with the hybrid electrolyte *vs.* 1.0 m Na₂SO_{4(aq)}, and it displays similar redox peaks in both electrolytes at *ca.* -0.95 V and -1.03 V *vs.* Ag/AgCl for the oxidation and reduction, respectively (Figure 28ac). The current density in 1.0 m Na₂SO_{4(aq)} is however only about half compared with the hybrid electrolyte, and the latter is clearly more reversible, but still, the redox peaks diminish significantly already after 3 cycles in both electrolytes. The charge/discharge curves are in agreement with the voltammogram for the hybrid electrolyte (Figure 28b), and NTP delivers *ca.* 120 mAh g⁻¹ in the initial cycle, similar to the original work [50]. Although, the electrode subsequently display severe capacity fading with low Coulombic efficiencies, as have been reported before due to Ti and P dissolution [55]. In contrast, the 1.0 m Na₂SO_{4(aq)} electrolyte-based cells failed completely to cycle (Figure 28d).

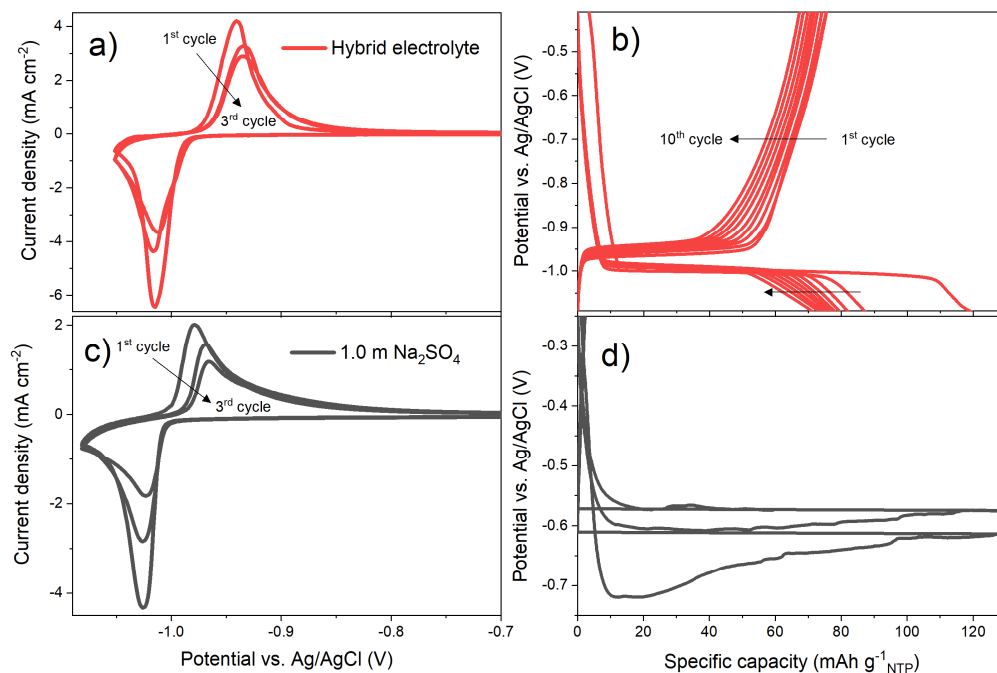


Figure 28. a,c) Voltammogram recorded at 0.2 mV s⁻¹ and b,d) GC charge/discharge curves of NTP electrodes at 0.2C.

NTP works with the hybrid electrolyte, albeit poorly, why attempts were made to enhance the stability; binders such as Na-alginate and PVDF were used instead of CMC; the graphite foil CC was swapped for Al; sodium dodecyl sulfate (SDS) was added the hybrid electrolyte; and finally, 0.1-0.2 m NaOH was added to the hybrid electrolyte to increase the pH to >12. Unfortunately, none of the above successfully improved the cycling stability – the only drawback hindering NTP from being a flawless ASIB/Na-HSC anode.

4.2.3 PTCDA

PTCDA was characterized by CV, GC, and EIS. The former shows the electrochemical response of PTCDA to have a drastic decrease in the current density with 1.0 m $\text{Na}_2\text{SO}_{4(\text{aq})}$ already after 10 cycles (Figure 29a). Whereas for the hybrid electrolyte much more stable and reversible cycling is obtained, with more than two times the current density (Figure 29b). The clear difference is most easily ascribed to the reduced solubility of Na_2PTCDA by the lower water concentration, witnessed for WISEs [31], and MgSO_4 might also improve the electrolyte stability during cycling.

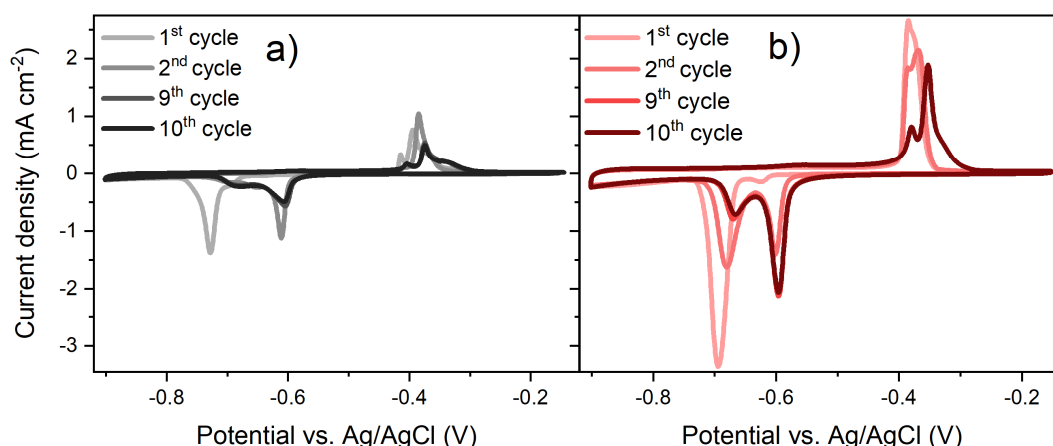


Figure 29. CV of PTCDA electrodes using the a) 1.0 m $\text{Na}_2\text{SO}_{4(\text{aq})}$ and b) hybrid electrolytes. (I).

In the first cycle, one redox peak during reduction is seen at *ca.* -0.7 V, and likewise one during oxidation, at *ca.* -0.4 V vs. Ag/AgCl for both electrolytes (Figure 29). This is very similar to what has been observed for PTCDA using non-aqueous electrolytes, where also, after an electrochemical conditioning process during the initial cycle(s) [31,60] *i.e.* an activation phase, the peaks are split into several consecutive, stable, redox peaks (Figure 29). In contrast, for PTCDA in aqueous electrolytes with other cations, the CVs differ either in the number of peaks and/or in the redox potentials [31,62,63]. Therefore, this strongly indicates that Na^+ is the primarily active cation in our electrolytes.

In accordance with the CVs, the GC charge/discharge profiles display extended voltage plateaus with the hybrid electrolyte, reaching initial discharge and charge capacities of 97 and 68 mAh g⁻¹, respectively (Figure 30b). A stable capacity of *ca.* 70 mAh g⁻¹ is thereafter achieved in excellent agreement with a two-electron reaction of PTCDA to Na_2PTCDA [60]. In stark contrast, most cells fail completely to cycle with 1.0 m $\text{Na}_2\text{SO}_{4(\text{aq})}$, and for the ones who do not, there are still severe problems already in the initial cycles (Figure 30a). This,

again, is attributed to PTCDA continuously being dissolved in the electrolyte due to the low salt concentration.

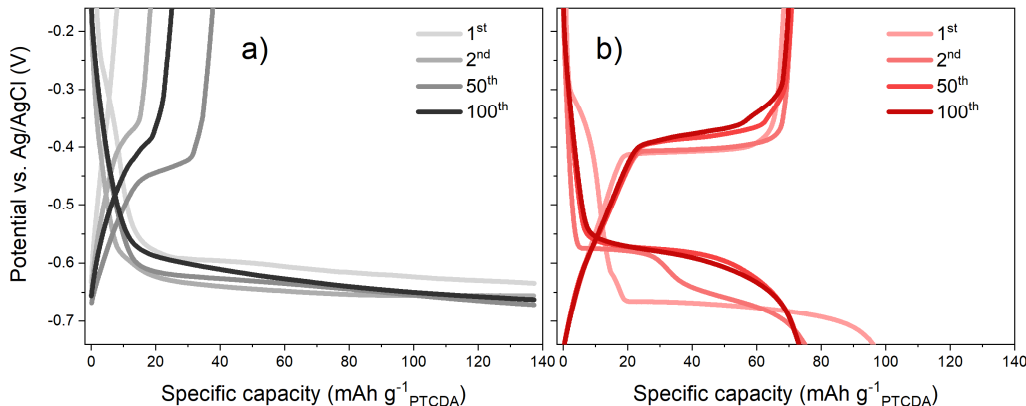


Figure 30. GC charge and discharge curves of PTCDA at 0.2C using a) the 1 m $\text{Na}_2\text{SO}_4(\text{aq})$ and b) the hybrid electrolytes. (I).

The rate capability tests reveal drastically impaired Coulombic efficiencies for the low C-rates with the 1 m Na_2SO_4 based electrolyte cells (Figure 31a, different y-axis). On the other hand, PTCDA with the hybrid electrolyte displays cells with remarkable rate capabilities and Coulombic efficiencies throughout the entire C-rate sweep, despite its much higher viscosity (Figure 31d). The 100 cycle tests also confirm the hybrid electrolyte to outperform 1 m Na_2SO_4 (Figure 31bcef), where the former displays high Coulombic efficiencies and capacity retentions at 0.2C, which further improves at 1C (Figure 31e). Our cells even outperform β -PTCDA with the 30 m KFSI WISE, using significantly higher current density (x14) which may hide/reduce parasitic reactions and contribute to the stability [31].

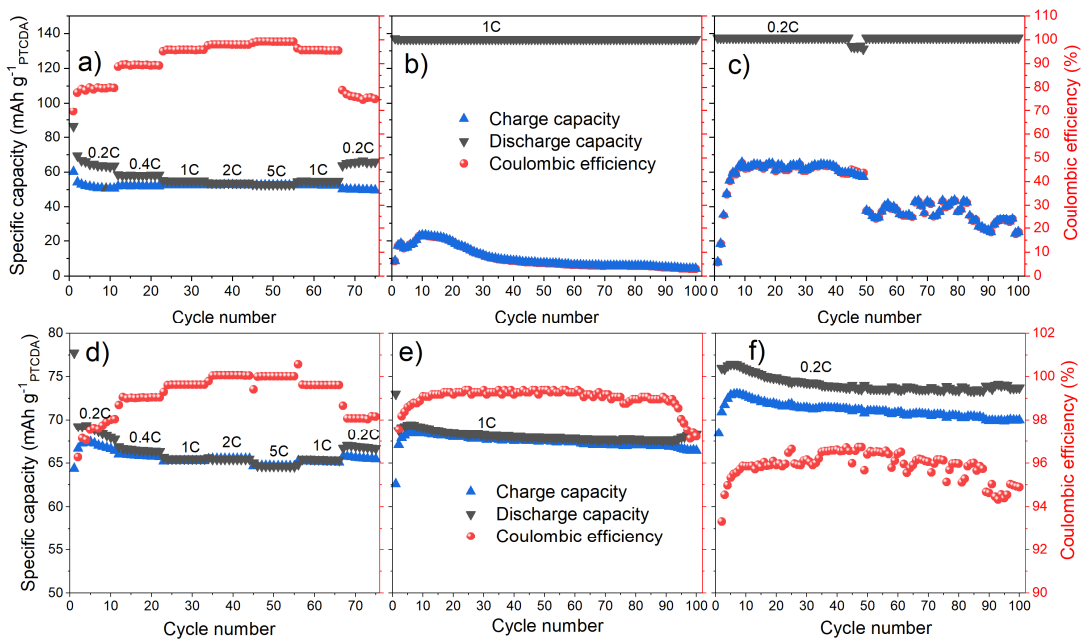


Figure 31. PTCDA electrode a,d) rate capability test and b,c,e,f) GC in a-c) 1 m $\text{Na}_2\text{SO}_4(\text{aq})$ and d-f) the hybrid electrolyte. Note the right and left y-axis scale differences between a-c and d-f. (I).

To validate whether suppressed dissolution of Na₂PTCDA is the cause of the clear outperformance, the separators were recovered from the cells after the 100 cycle GC test. Indeed, no sign of any red colour indicating reduced and dissolved PTCDA [62,63] is seen on the separators with the hybrid electrolyte (Figure 32ab), quite unlike the situation with 1 m Na₂SO_{4(aq)} (Figure 32cd). A discharged PTCDA electrode was also immersed in water, dyeing the water dark red, verifying the polarity increase of PTCDA in its reduced state (Figure 32e). The separators were further immersed in 1 ml 2 m NaOH, where dissolved PTCDA turns green when the structure is destroyed by OH⁻ [31,62]. Again, the separators from the hybrid electrolyte cells remain colourless (Figure 32f), confirming the suppressed dissolution of Na₂PTCDA.

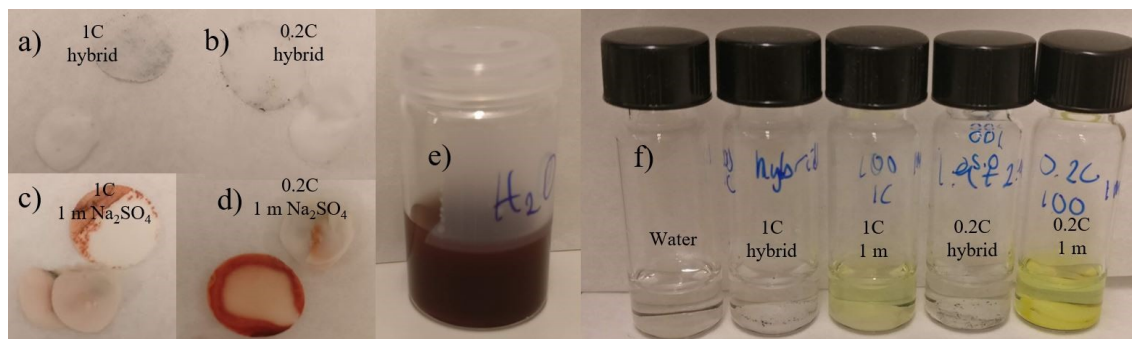


Figure 32. a-d) Separators after 100 galvanostatic cycles. The smaller, cut separators were barriers to the RE and the black ‘dirt’ originates from the AC CE. e) A PTCDA electrode discharged to -0.8 V vs. Ag/AgCl then put in water. f) Separators after a couple of days in 1 ml 2 m NaOH. (I).

The lower water concentration probably has a notable effect in the hybrid electrolyte, but Yue *et al.* also showed that the dissolution kinetics are highly dependent on the viscosity [104], which is very reasonable since the dissolved active material needs to be transported away as the electrode/electrolyte interface becomes saturated.

4.3 All-organic aqueous energy storage devices

4.3.1 PTCDA//AC

To make use of the great PTCDA rate capability, PTCDA//AC Na-HSCs were assembled with a *ca.* 1:3 PTCDA:AC weight ratio to balance the capacity of the electrodes. The ESD provide a stable capacity of *ca.* 22 mAh g⁻¹_{AC+PTCDA} at 0.5 A g⁻¹ after the activation process, and it also displays a very good cycling stability; 86% capacity retention from the 10th to the 1000th cycle at 1 A g⁻¹, with a Coulombic efficiency >98% (Figure 33ab). This is on par with or exceeds that of the best comparable high-performant “all-organic” aqueous ESDs in the literature [58,66,73,75,77]. From the Nyquist plot, and by implementing the simple and commonly used Randles circuit cell model, the charge-transfer resistance (R_{ct} , 18.3 Ω cm⁻²) and the electrolyte resistance (R_s , 2.1 Ω cm⁻²) were extracted at OCV before cycling (Figure 33d). The former drastically decreases ($R_{ct, final}$, 7.8 Ω cm⁻²) while the latter stays relatively constant after cycling. In comparison, a PDI-Ph//ATA battery had resistances ($R_{ct, initial}$ = 53

Ω , $R_{s, initial} = 1.86 \Omega$) which both slightly increased after cycling [71]. As we here use 10 mm \varnothing electrodes, the resistance unit difference need not be taking into account ($1 \Omega \leftrightarrow 1.27 \Omega \text{ cm}^{-2}$). Thus, the Na-HSC has very good charge transport kinetics and conductivity. Unfortunately, no other EIS measurements of all-organic aqueous energy storage devices in full cell configurations were found in the literature.

The energy and power densities are for the Na-HSC 16.7 Wh kg^{-1} (at 0.5 A g^{-1}) and 19.0 kW kg^{-1} (at 50 A g^{-1}), respectively. The former does – by no means – surpass the state-of-the-art ASIBs or aqueous sodium-ion supercapacitor (Figure 33c) [105–107] and offer merely a quarter of the energy density previously reported for an “all-organic” aqueous Na-HSC (Table 1). The power density is, however, surprisingly high as it almost reaches what have been previously reported for an aqueous Na-ion supercapacitor (20 kW kg^{-1} [106]). The energy efficiency, was calculated to 76%, slightly below conventional LIB layered oxide cathodes [108], but higher than LIB anodes and supercapacitors [109], and therefore should not be a limiting factor for practical implementation.

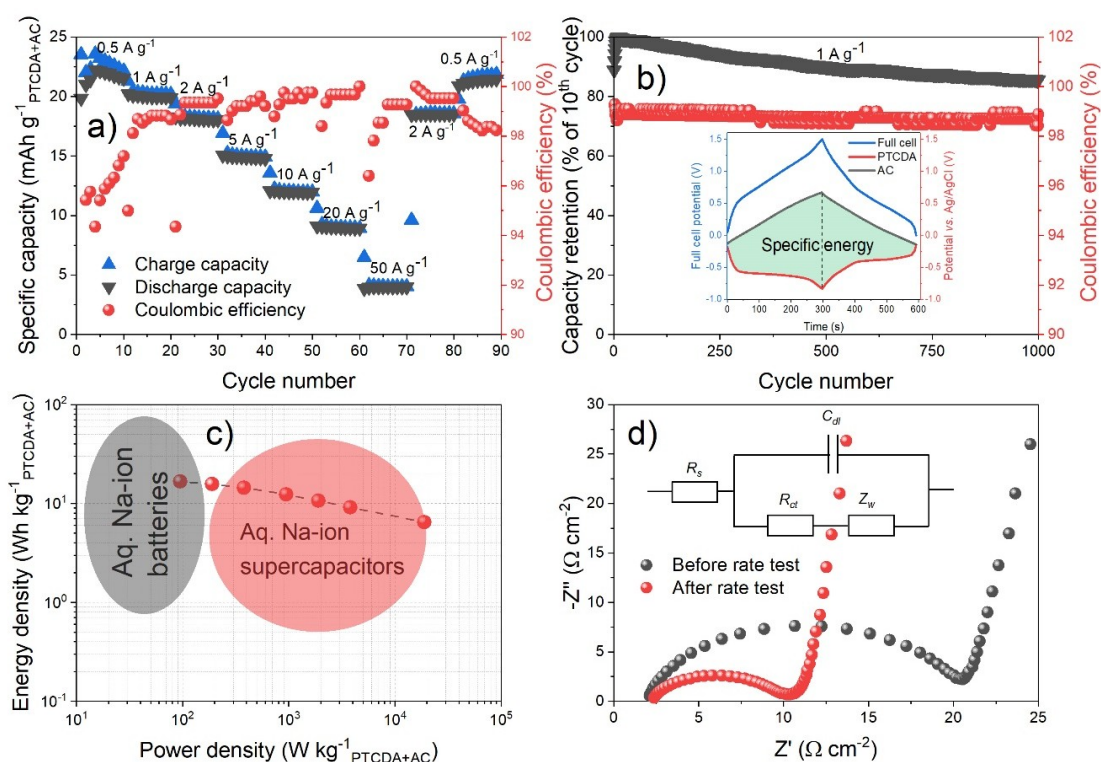


Figure 33. a) Rate capability test, b) GC stability test, c) Ragone plot, and d) Nyquist plot of the Na-HSC with the Randles circuit. Inset in (b) shows the corresponding charge/discharge curves of the 100th cycle. (II).

From the technical performance, we now turn to the sustainability and cost, both of which are difficult to estimate/quantify. Still, relative comparisons are possible. First and foremost, the cost of aqueous electrolytes are easily estimated by comparing the raw material prices of similar sized batches with similar purities of the salt(s) used [110]. The hybrid electrolyte is made from elements very common in minerals in the Earth’s crust, and the use of non-fluorinated/non-

perchlorate salts not only drastically lowers the price tag, but also render the materials synthesis less environmentally unfriendly [7,26]. Moreover, by using organic CCs, the large environmental footprint and cost from the mining and production of metals are avoided [111–115]. Cellulose separators are not laden with the large GHG emissions (CO₂, CO, SO_x, and NO_x) of glass fiber and polyolefin based (oil-derived) separators [116]. Also, by refraining from using PVDF, NMP can be replaced with water, reducing cost and CO₂ emissions [117]. Furthermore, the active materials; PTCDA and AC (as well as the binder, separator, salts, and CCs) are commercially available, at a low cost, and thus do not require complicated synthesis protocols, which might be one of the most critical factors when considering cost and energy use. Finally, there is no need or incentive to recycle the all-organic ESD, and it can easily be disposed of as organic waste after EOL.

Therefore, in summary, the presented all-organic aqueous Na-HSC takes unprecedented steps towards creating the low-cost and low environmental impact device needed for truly sustainable energy storage.

5. Conclusions & Outlook

The novel aqueous “hybrid” electrolyte based on sodium and magnesium sulfate salts displays promising and similar properties as WISEs. It also enables slow C-rate cycling of NTP and Fennac electrodes, with significantly improved electrochemical performance of the latter. Moreover, the hybrid electrolyte – for the first time – enables high-performant PTCDA electrodes for aqueous Na-ion ESDs by suppressing active material dissolution. Most notably, the electrode exhibits excellent power capabilities, wherefore all-organic aqueous PTCDA//AC Na-HSCs of exclusively commercial materials were assembled, and the ESDs proves to be a great alternative for safe, low-cost, and sustainable energy storage with adequate technical performance.

Naturally, the hybrid electrolyte is not flawless, and cycling instabilities of NTP still remain. Going forward, an electrolyte of several salts, surfactants, and possibly sugars, could have synergistic effects to increase the ESW of $\text{Na}_2\text{SO}_{4(\text{aq})}$ and decrease active material dissolution.

Although the excellent properties and advantages of AC (cost, sustainability, electrochemical performance, *etc.*) it is undeniably a bottle neck towards high energy densities. Low PTCDA mass loadings render capacities close to 90 mAh g^{-1} , more than 3 times that of AC. Thus, finding an alternative high capacity, and/or high voltage cathode active material could greatly improve the energy density and make the ESD even more applicable. The restrictions are, however, many, as it needs to be commercially available, compatible with aqueous electrolytes, able to reversible intercalate Na^+ , redox active between *ca.* 0.4 V and 1 V *vs.* Ag/AgCl, fluorine-free, and of course, organic (possibly Fe/Ti). The overlapping Venndiagram is not large, but a couple of promising polymeric materials exist, both of which have been well studied, but they still could prove successful in making energy denser PTCDA-based ESDs.

6. Acknowledgements

First of all, I would like to express my appreciation towards the Swedish Research Council for Sustainable Development (FORMAS) for supporting this work.

I very much thank my supervisor Prof. Patrik Johansson for giving me the opportunity to be a part of this excellent research group, for giving me the freedom and resources to pursue my ideas, and for supporting me with knowledge and insight in the academic world.

I would also like to give a special thank you to Dr. Roza Bouchal and Dr. Ezio Zanghellini, for helping me getting started, for your expertise, your patience and for always helping me in the lab, even though I am sometimes not the best listener... I could not have done this without you!

A shoutout to my great colleagues for making the weeks fly by, for putting up with me and my stupid jokes, and of course to my friends for making this life very enjoyable, green light is the only light!

Finally, to my family, whom I never see nearly enough. *Thank you* for all the love and support throughout the years. I even miss you nowadays, and I am truly grateful for everything.

7. Bibliography

- [1] S. Wang, Q. Li, C. Fang, C. Zhou, The relationship between economic growth, energy consumption, and CO₂ emissions: Empirical evidence from China, *Sci. Total Environ.* 542 (2016) 360–371.
- [2] UN, *Transforming Our World by 2030: A New Agenda For Global Action*, 2015.
- [3] B. Dunn, H. Kamath, J.M. Tarascon, Electrical energy storage for the grid: A battery of choices, *Science* (80-.). 334 (2011) 928–935.
- [4] H. Pan, Y.S. Hu, L. Chen, Room-temperature stationary sodium-ion batteries for large-scale electric energy storage, *Energy Environ. Sci.* 6 (2013) 2338–2360.
- [5] G.A. Blengini, C.E.L. Latunussa, U. Eynard, C. Torres de Matos, D. Wittmer, K. Georgitzikis, C. Pavel, S. Carrara, L. Mancini, M. Unguru, D. Blagoeva, F. Mathieux, D. Pennington, *Study on the EU’s list of Critical Raw Materials (2020) Final Report*, Publications Office of the European Union, 2020.
- [6] Democratic Republic of Congo: “This is what we die for”: Human rights abuses in the Democratic Republic of the Congo power the global trade in cobalt | Amnesty International, (n.d.). <https://www.amnesty.org/en/documents/afr62/3183/2016/en/> (accessed September 8, 2021).
- [7] L.J. Vimmerstedt, S. Ring, C.J. Hammel, *Current status of environmental, health, and safety issues of lithium ion electric vehicle batteries*, Golden, CO, 1995.
- [8] A. Hammami, N. Raymond, M. Armand, Runaway risk of forming toxic compounds, *Nat.* 2003 4246949. 424 (2003) 635–636.
- [9] N. Tapia-Ruiz *et al.*, 2021 roadmap for sodium-ion batteries, *J. Phys. Energy.* 3 (2021) 031503.
- [10] V.A. Oltean, S. Renault, M. Valvo, D. Brandell, Sustainable materials for sustainable energy storage: Organic Na electrodes, *Materials (Basel).* 9 (2016).
- [11] A. Richelli, M. Salem, L. Colalongo, A Review of Fully Integrated and Embedded Power Converters for IoT, *Energies* 2021, Vol. 14, Page 5419. 14 (2021) 5419.
- [12] *Oxford Dictionary of English*, Oxford Dict. English. (2010).
- [13] A. Rudola, A.J.R. Rennie, R. Heap, S.S. Meysami, A. Lowbridge, F. Mazzali, R. Sayers, C.J. Wright, J. Barker, Commercialisation of high energy density sodium-ion batteries: Faradion’s journey and outlook, *J. Mater. Chem. A.* 9 (2021) 8279–8302.
- [14] K. Krishnamoorthy, P. Pazhamalai, S. Sahoo, J.H. Lim, K.H. Choi, S.J. Kim, A High-Energy Aqueous Sodium-Ion Capacitor with Nickel Hexacyanoferrate and Graphene Electrodes, *ChemElectroChem.* 4 (2017) 3302–3308.

- [15] A. González, E. Goikolea, J.A. Barrena, R. Mysyk, Review on supercapacitors: Technologies and materials, *Renew. Sustain. Energy Rev.* 58 (2016) 1189–1206.
- [16] B. Zhao, D. Chen, X. Xiong, B. Song, R. Hu, Q. Zhang, B.H. Rainwater, G.H. Waller, D. Zhen, Y. Ding, Y. Chen, C. Qu, D. Dang, C.P. Wong, M. Liu, A high-energy, long cycle-life hybrid supercapacitor based on graphene composite electrodes, *Energy Storage Mater.* 7 (2017) 32–39.
- [17] N. Yabuuchi, K. Kubota, M. Dahbi, S. Komaba, Research development on sodium-ion batteries, *Chem. Rev.* 114 (2014) 11636–11682.
- [18] K. Chayambuka, G. Mulder, D.L. Danilov, P.H.L. Notten, Sodium-Ion Battery Materials and Electrochemical Properties Reviewed, *Adv. Energy Mater.* 8 (2018) 1800079.
- [19] A. Rudola, A.J.R. Rennie, R. Heap, S.S. Meysami, A. Lowbridge, F. Mazzali, R. Sayers, C.J. Wright, J. Barker, Commercialisation of high energy density sodium-ion batteries: Faradion’s journey and outlook, *J. Mater. Chem. A.* 9 (2021) 8279–8302.
- [20] Smart Sodium Storage System - Australian Renewable Energy Agency (ARENA), (2016). <https://arena.gov.au/projects/smart-sodium-storage-system-for-renewable-energy-storage/> (accessed December 2, 2021).
- [21] Z. Nannan, China First Demonstrates the 100 kWh Na-Ion Battery System for Energy Storage, *Chinese Acad. Sci.* (2019). https://english.cas.cn/newsroom/research_news/201904/t20190401_207399.shtml (accessed December 2, 2021).
- [22] Y. Cao, L. Xiao, W. Wang, D. Choi, Z. Nie, J. Yu, L. V. Saraf, Z. Yang, J. Liu, Reversible Sodium Ion Insertion in Single Crystalline Manganese Oxide Nanowires with Long Cycle Life, *Adv. Mater.* 23 (2011) 3155–3160.
- [23] A. Bauer, J. Song, S. Vail, W. Pan, J. Barker, Y. Lu, The Scale-up and Commercialization of Nonaqueous Na-Ion Battery Technologies, *Adv. Energy Mater.* 8 (2018) 1702869.
- [24] R. Mogensen, A. Buckel, S. Colbin, R. Younesi, A Wide-Temperature-Range, Low-Cost, Fluorine-Free Battery Electrolyte Based on Sodium Bis(Oxalate)Borate, *Chem. Mater.* 33 (2021) 1130–1139.
- [25] S.E. Sloop, J.K. Pugh, S. Wang, J.B. Kerr, K. Kinoshita, Chemical Reactivity of PF₅ and LiPF₆ in Ethylene Carbonate/Dimethyl Carbonate Solutions, *Electrochem. Solid-State Lett.* 4 (2001) A42.
- [26] G.L. Henriksen, K. Amine, J. Liu, Materials cost evaluation report for high-power Li-ion batteries., Argonne, IL (United States), 2003.
- [27] D. Pahari, S. Puravankara, Greener, Safer, and Sustainable Batteries: An Insight into Aqueous Electrolytes for Sodium-Ion Batteries, *ACS Sustain. Chem. Eng.* 8 (2020) 10613–10625.

- [28] L. Suo, O. Borodin, T. Gao, M. Olguin, J. Ho, X. Fan, C. Luo, C. Wang, K. Xu, “Water-in-salt” electrolyte enables high-voltage aqueous lithium-ion chemistries, *Science* (80-.). 350 (2015) 938–943.
- [29] Y. Yamada, K. Usui, K. Sodeyama, S. Ko, Y. Tateyama, A. Yamada, Hydrate-melt electrolytes for high-energy-density aqueous batteries, *Nat. Energy*. 1 (2016) 1–9.
- [30] Y. Yamada, K. Furukawa, K. Sodeyama, K. Kikuchi, M. Yaegashi, Y. Tateyama, A. Yamada, Unusual stability of acetonitrile-based superconcentrated electrolytes for fast-charging lithium-ion batteries, *J. Am. Chem. Soc.* 136 (2014) 5039–5046.
- [31] H. Chen, Z. Zhang, Z. Wei, G. Chen, X. Yang, C. Wang, F. Du, Use of a water-in-salt electrolyte to avoid organic material dissolution and enhance the kinetics of aqueous potassium ion batteries, *Sustain. Energy Fuels*. 4 (2019) 128–131.
- [32] L. Jiang *et al.*, Building aqueous K-ion batteries for energy storage, *Nat. Energy*. 4 (2019) 495–503.
- [33] Z. Song, H. Zhou, Towards sustainable and versatile energy storage devices: an overview of organic electrode materials, *Energy Environ. Sci.* 6 (2013) 2280–2301.
- [34] W. Deng, Y. Shen, J. Qian, H. Yang, A polyimide anode with high capacity and superior cyclability for aqueous Na-ion batteries, *Chem. Commun.* 51 (2015) 5097–5099.
- [35] O. Borodin, J. Self, K.A. Persson, C. Wang, K. Xu, Uncharted Waters: Super-Concentrated Electrolytes, *Joule*. 4 (2020) 69–100.
- [36] K. Xu, Nonaqueous liquid electrolytes for lithium-based rechargeable batteries, *Chem. Rev.* 104 (2004) 4303–4417.
- [37] M.R. Lukatskaya, J.I. Feldblyum, D.G. Mackanic, F. Lissel, D.L. Michels, Y. Cui, Z. Bao, Concentrated mixed cation acetate “water-in-salt” solutions as green and low-cost high voltage electrolytes for aqueous batteries, *Energy Environ. Sci.* 11 (2018) 2876–2883.
- [38] J. Han, H. Zhang, A. Varzi, S. Passerini, Fluorine-Free Water-in-Salt Electrolyte for Green and Low-Cost Aqueous Sodium-Ion Batteries, *ChemSusChem*. 11 (2018) 3704–3707.
- [39] J.F. Whitacre, A. Tevar, S. Sharma, Na₄Mn₉O₁₈ as a positive electrode material for an aqueous electrolyte sodium-ion energy storage device, *Electrochem. Commun.* 12 (2010) 463–466.
- [40] J.F. Whitacre, T. Wiley, S. Shanbhag, Y. Wenzhuo, A. Mohamed, S.E. Chun, E. Weber, D. Blackwood, E. Lynch-Bell, J. Gulakowski, C. Smith, D. Humphreys, An aqueous electrolyte, sodium ion functional, large format energy storage device for stationary applications, *J. Power Sources*. 213 (2012) 255–264.
- [41] Q. Zhang, C. Liao, T. Zhai, H. Li, A High Rate 1.2V Aqueous Sodium-ion Battery Based on All NASICON Structured NaTi₂(PO₄)₃ and Na₃V₂(PO₄)₃, *Electrochim. Acta*. 196

(2016) 470–478.

- [42] D. Bin, F. Wang, A.G. Tamirat, L. Suo, Y. Wang, C. Wang, Y. Xia, Progress in Aqueous Rechargeable Sodium-Ion Batteries, *Adv. Energy Mater.* 8 (2018) 1703008.
- [43] H. Wang, T. Zhang, C. Chen, M. Ling, Z. Lin, S. Zhang, F. Pan, C. Liang, High-performance aqueous symmetric sodium-ion battery using NASICON-structured $\text{Na}_2\text{VTi}(\text{PO}_4)_3$, *Nano Res.* 2018 111. 11 (2017) 490–498.
- [44] H. Gao, J.B. Goodenough, An Aqueous Symmetric Sodium-Ion Battery with NASICON-Structured $\text{Na}_3\text{MnTi}(\text{PO}_4)_3$, *Angew. Chemie - Int. Ed.* 55 (2016) 12768–12772.
- [45] S. Qiu, Y. Xu, X. Wu, X. Ji, Prussian Blue Analogues as Electrodes for Aqueous Monovalent Ion Batteries, *Electrochem. Energy Rev.* 1 (2021) 3.
- [46] C. Ling, J. Chen, F. Mizuno, First-principles study of alkali and alkaline earth ion intercalation in iron hexacyanoferrate: The important role of ionic radius, *J. Phys. Chem. C.* 117 (2013) 21158–21165.
- [47] X. Wu, M. Sun, S. Guo, J. Qian, Y. Liu, Y. Cao, X. Ai, H. Yang, Vacancy-Free Prussian Blue Nanocrystals with High Capacity and Superior Cyclability for Aqueous Sodium-Ion Batteries, *ChemNanoMat.* 1 (2015) 188–193.
- [48] L. Zhou, Z. Yang, C. Li, B. Chen, Y. Wang, L. Fu, Y. Zhu, X. Liu, Y. Wu, Prussian blue as positive electrode material for aqueous sodium-ion capacitor with excellent performance, *RSC Adv.* 6 (2016) 109340–109345.
- [49] A.J. Fernández-Ropero, M.J. Piernas-Muñoz, E. Castillo-Martínez, T. Rojo, M. Casas-Cabanas, Electrochemical characterization of $\text{NaFe}_2(\text{CN})_6$ Prussian Blue as positive electrode for aqueous sodium-ion batteries, *Electrochim. Acta.* 210 (2016) 352–357.
- [50] S. Il Park, I. Gocheva, S. Okada, J. Yamaki, Electrochemical Properties of $\text{NaTi}_2(\text{PO}_4)_3$ Anode for Rechargeable Aqueous Sodium-Ion Batteries, *J. Electrochem. Soc.* 158 (2011) A1067.
- [51] K. Chayambuka, G. Mulder, D.L. Danilov, P.H.L. Notten, Sodium-Ion Battery Materials and Electrochemical Properties Reviewed, *Adv. Energy Mater.* 8 (2018) 1800079.
- [52] W. Wu, J. Yan, A. Wise, A. Rutt, J.F. Whitacre, Using Intimate Carbon to Enhance the Performance of $\text{NaTi}_2(\text{PO}_4)_3$ Anode Materials: Carbon Nanotubes vs Graphite, *J. Electrochem. Soc.* 161 (2014) A561–A567.
- [53] S. Zhang, Y. Liu, Q. Han, S. He, N. Zhang, J. Yang, Development and characterization of aqueous sodium-ion hybrid supercapacitor based on $\text{NaTi}_2(\text{PO}_4)_3$ /activated carbon, *J. Alloys Compd.* 729 (2017) 850–857.
- [54] J.Y. Luo, W.J. Cui, P. He, Y.Y. Xia, Raising the cycling stability of aqueous lithium-ion batteries by eliminating oxygen in the electrolyte, *Nat. Chem.* 2 (2010) 760–765.

- [55] G. Plečkaitytė, M. Petrulevičienė, L. Staišiūnas, D. Tediashvili, J. Pilipavičius, J. Juodkazytė, L. Vilčiauskas, Understanding and mitigation of $\text{NaTi}_2(\text{PO}_4)_3$ degradation in aqueous Na-ion batteries, *J. Mater. Chem. A*. 9 (2021) 12670–12683.
- [56] Y. Liu, B.H. Zhang, S.Y. Xiao, L.L. Liu, Z.B. Wen, Y.P. Wu, A nanocomposite of MoO_3 coated with PPy as an anode material for aqueous sodium rechargeable batteries with excellent electrochemical performance, *Electrochim. Acta*. 116 (2014) 512–517.
- [57] M. Pasta, C.D. Wessells, N. Liu, J. Nelson, M.T. McDowell, R.A. Huggins, M.F. Toney, Y. Cui, Full open-framework batteries for stationary energy storage, *Nat. Commun.* 2014 51. 5 (2014) 1–9.
- [58] Y. Zhang, P. Nie, C. Xu, G. Xu, B. Ding, H. Dou, X. Zhang, High energy aqueous sodium-ion capacitor enabled by polyimide electrode and high-concentrated electrolyte, *Electrochim. Acta*. 268 (2018) 512–519.
- [59] X. Han, C. Chang, L. Yuan, T. Sun, J. Sun, Aromatic carbonyl derivative polymers as high-performance Li-ion storage materials, *Adv. Mater.* 19 (2007) 1616–1621.
- [60] W. Luo, M. Allen, V. Raju, X. Ji, An Organic Pigment as a High-Performance Cathode for Sodium-Ion Batteries, *Adv. Energy Mater.* 4 (2014) 1400554.
- [61] M. Möbus, N. Karl, T. Kobayashi, Structure of perylene-tetracarboxylic-dianhydride thin films on alkali halide crystal substrates, *J. Cryst. Growth*. 116 (1992) 495–504.
- [62] X. Wang, C. Bommier, Z. Jian, Z. Li, R.S. Chandrabose, I.A. Rodríguez-Pérez, P.A. Greaney, X. Ji, Hydronium-Ion Batteries with Perylenetetracarboxylic Dianhydride Crystals as an Electrode, *Angew. Chemie Int. Ed.* 56 (2017) 2909–2913.
- [63] I.A. Rodríguez-Pérez, Y. Yuan, C. Bommier, X. Wang, L. Ma, D.P. Leonard, M.M. Lerner, R.G. Carter, T. Wu, P.A. Greaney, J. Lu, X. Ji, Mg-Ion Battery Electrode: An Organic Solid's Herringbone Structure Squeezed upon Mg-Ion Insertion, *J. Am. Chem. Soc.* 139 (2017) 13031–13037.
- [64] X. Yin, S. Sarkar, S. Shi, Q.A. Huang, H. Zhao, L. Yan, Y. Zhao, J. Zhang, Recent Progress in Advanced Organic Electrode Materials for Sodium-Ion Batteries: Synthesis, Mechanisms, Challenges and Perspectives, *Adv. Funct. Mater.* 1908445 (2020) 1–21.
- [65] J. Huang, X. Dong, Z. Guo, Y. Wang, Progress of Organic Electrodes in Aqueous Electrolyte for Energy Storage and Conversion, *Angew. Chemie.* (2020) ange.202003198.
- [66] Y. Zhang, Y. An, L. Wu, H. Chen, Z. Li, H. Dou, V. Murugadoss, J. Fan, X. Zhang, X. Mai, Z. Guo, Metal-free energy storage systems: combining batteries with capacitors based on a methylene blue functionalized graphene cathode, *J. Mater. Chem. A*. 7 (2019) 19668–19675.
- [67] Y. Xu, M. Zhou, Y. Lei, Organic materials for rechargeable sodium-ion batteries, *Mater. Today*. 21 (2018) 60–78.

- [68] H.J. Becker, Low voltage electrolytic capacitor, 2800616, U.S. Patent Office (1954).
- [69] H. Lu, X.S. Zhao, Biomass-derived carbon electrode materials for supercapacitors, *Sustain. Energy Fuels*. 1 (2017) 1265–1281.
- [70] S. Lindberg, N.M. Ndiaye, N. Manyala, P. Johansson, A. Matic, A VO₂ based hybrid super-capacitor utilizing a highly concentrated aqueous electrolyte for increased potential window and capacity, *Electrochim. Acta*. 345 (2020) 136225.
- [71] K.C.S. Lakshmi, X. Ji, T.-Y. Chen, B. Vedhanarayanan, T.-W. Lin, Pseudocapacitive and battery-type organic polymer electrodes for a 1.9 V hybrid supercapacitor with a record concentration of ammonium acetate, *J. Power Sources*. 511 (2021) 230434.
- [72] T. Tomai, S. Mitani, D. Komatsu, Y. Kawaguchi, I. Honma, Metal-free aqueous redox capacitor via proton rocking-chair system in an organic-based couple, *Sci. Reports* 2014 41. 4 (2014) 1–6.
- [73] X. Dong, H. Yu, Y. Ma, J.L. Bao, D.G. Truhlar, Y. Wang, Y. Xia, All-Organic Rechargeable Battery with Reversibility Supported by “Water-in-Salt” Electrolyte, *Chem. – A Eur. J.* 23 (2017) 2560–2565.
- [74] Z. Khan, U. Ail, F.N. Ajjan, J. Phopase, Z.U. Khan, N. Kim, J. Nilsson, O. Inganäs, M. Berggren, X. Crispin, Water-in-Polymer Salt Electrolyte for Slow Self-Discharge in Organic Batteries, *Adv. Energy Sustain. Res.* 3 (2022) 2100165.
- [75] N. Patil, A. Mavrandonakis, C. Jérôme, C. Detrembleur, N. Casado, D. Mecerreyes, J. Palma, R. Marcilla, High-performance all-organic aqueous batteries based on a poly(imide) anode and poly(catechol) cathode, *J. Mater. Chem. A*. 9 (2021) 505–514.
- [76] Y. Xu, Y. Zheng, C. Wang, Q. Chen, An All-Organic Aqueous Battery Powered by Adsorbed Quinone, *ACS Appl. Mater. Interfaces*. 11 (2019) 23222–23228.
- [77] Yadi Zhang, Yufeng An, Bo Yin, Jiangmin Jiang, Shengyang Dong, Hui Dou, Xiaogang Zhang, A novel aqueous ammonium dual-ion battery based on organic polymers, *J. Mater. Chem. A*. 7 (2019) 11314–11320.
- [78] N. Sano, W. Tomita, S. Hara, C.-M. Min, J.-S. Lee, K. Oyaizu, H. Nishide, Polyviologen Hydrogel with High-Rate Capability for Anodes toward an Aqueous Electrolyte-Type and Organic-Based Rechargeable Device, *ACS Appl. Mater. Interfaces*. 5 (2013) 1355–1361.
- [79] K. Hatakeyama-Sato, H. Wakamatsu, K. Yamagishi, T. Fujie, S. Takeoka, K. Oyaizu, H. Nishide, Ultrathin and Stretchable Rechargeable Devices with Organic Polymer Nanosheets Conformable to Skin Surface, *Small*. 15 (2019) 1805296.
- [80] Z. Algharaibeh, P.G. Pickup, An asymmetric supercapacitor with anthraquinone and dihydroxybenzene modified carbon fabric electrodes, *Electrochem. Commun.* 13 (2011) 147–149.
- [81] K. -D Kreuer, A. Rabenau, W. Weppner, Vehicle Mechanism, A New Model for the

- Interpretation of the Conductivity of Fast Proton Conductors, *Angew. Chemie Int. Ed. English*. 21 (1982) 208–209.
- [82] P. Walden, Über organische Lösungs und Ionisierungsmittel. III. Teil: Innere Reibung und deren Zusammenhang mit dem Leitvermögen, *Zeitschrift Für Phys. Chemie*. 55 (1906) 207–246.
- [83] W. Xu, E.I. Cooper, C.A. Angell, *Ionic Liquids: Ion Mobilities, Glass Temperatures, and Fragilities*, (2003).
- [84] J.R. Ferraro, K. Nakamoto, C.W. Brown, *Introductory Raman Spectroscopy*, (2003).
- [85] Q. Sun, The Raman OH stretching bands of liquid water, *Vib. Spectrosc.* 51 (2009) 213–217.
- [86] J.D. Benck, B.A. Pinaud, Y. Gorlin, T.F. Jaramillo, Substrate selection for fundamental studies of electrocatalysts and photoelectrodes: Inert potential windows in acidic, neutral, and basic electrolyte, *PLoS One*. 9 (2014) e107942.
- [87] F. Scholz, *Electroanalytical methods: Guide to experiments and applications*, *Electroanal. Methods Guid. to Exp. Appl.* (2010) 1–359.
- [88] J.N. Scott, N. V. Nucci, J.M. Vanderkooi, Changes in water structure induced by the guanidinium cation and implications for protein denaturation, *J. Phys. Chem. A*. 112 (2008) 10939–10948.
- [89] F.P. Daly, C.W. Brown, D.R. Kester, F.P. Daly, C.W. Brown, D.R. Kester, Sodium and Magnesium Sulfate Ion Pairing: Evidence from Raman Spectroscopy, n.d. <https://pubs.acs.org/sharingguidelines> (accessed February 25, 2020).
- [90] R.J. Sension, B. Hudson, P.R. Callis, Resonance raman studies of guanidinium and substituted guanidinium ions, *J. Phys. Chem.* 94 (1990) 4015–4025.
- [91] J. Han, M. Zarrabeitia, A. Mariani, Z. Jusys, M. Hekmatfar, H. Zhang, D. Geiger, U. Kaiser, R.J. Behm, A. Varzi, S. Passerini, Halide-free water-in-salt electrolytes for stable aqueous sodium-ion batteries, *Nano Energy*. 77 (2020) 105176.
- [92] L. Niu, L. Chen, J. Zhang, P. Jiang, Z. Liu, Revisiting the open-framework zinc hexacyanoferrate: The role of ternary electrolyte and sodium-ion intercalation mechanism, *J. Power Sources*. 380 (2018) 135–141.
- [93] T. Li, M. Li, H. Li, H. Zhao, High-voltage and long-lasting aqueous chlorine-ion battery by virtue of “water-in-salt” electrolyte, *IScience*. 24 (2021).
- [94] M.H. Lee, S.J. Kim, D. Chang, J. Kim, S. Moon, K. Oh, K.Y. Park, W.M. Seong, H. Park, G. Kwon, B. Lee, K. Kang, Toward a low-cost high-voltage sodium aqueous rechargeable battery, *Mater. Today*. 29 (2019) 26–36.
- [95] D. Reber, R. Figi, R.S. Kühnel, C. Battaglia, Stability of aqueous electrolytes based on LiFSI and NaFSI, *Electrochim. Acta*. 321 (2019) 134644.

- [96] D. Reber, R.S. Kühnel, C. Battaglia, High-voltage aqueous supercapacitors based on NaTFSI, *Sustain. Energy Fuels*. 1 (2017) 2155–2161.
- [97] M.B. Herath, S.E. Creager, A. Kitaygorodskiy, D.D. DesMarteau, Perfluoroalkyl Phosphonic and Phosphinic Acids as Proton Conductors for Anhydrous Proton-Exchange Membranes, *ChemPhysChem*. 11 (2010) 2871–2878.
- [98] A. Dave, K.L. Gering, J.M. Mitchell, J. Whitacre, V. Viswanathan, Benchmarking Conductivity Predictions of the Advanced Electrolyte Model (AEM) for Aqueous Systems, *J. Electrochem. Soc.* 167 (2020) 013514.
- [99] Q. Zheng *et al.*, Sodium- and Potassium-Hydrate Melts Containing Asymmetric Imide Anions for High-Voltage Aqueous Batteries, *Angew. Chemie Int. Ed.* 58 (2019) 14202–14207.
- [100] M. Mcln, C.A. Angeli, Contrasting Conductance/Viscosity Relations in Liquid States of Vitreous and Polymer “Solid” Electrolytes, 1988. <https://pubs.acs.org/sharingguidelines> (accessed February 19, 2021).
- [101] H. Bi *et al.*, J. Chen, A Universal Approach to Aqueous Energy Storage via Ultralow-Cost Electrolyte with Super-Concentrated Sugar as Hydrogen-Bond-Regulated Solute, *Adv. Mater.* 32 (2020) 2000074.
- [102] Z. Hou, X. Zhang, X. Li, Y. Zhu, J. Liang, Y. Qian, Surfactant widens the electrochemical window of an aqueous electrolyte for better rechargeable aqueous sodium/zinc battery, *J. Mater. Chem. A*. 5 (2017) 730–738.
- [103] M.M. Huie, D.C. Bock, E.S. Takeuchi, A.C. Marschilok, K.J. Takeuchi, Cathode materials for magnesium and magnesium-ion based batteries, *Coord. Chem. Rev.* 287 (2015) 15–27.
- [104] J. Yue, L. Lin, L. Jiang, Q. Zhang, Y. Tong, L. Suo, Y. Hu, H. Li, X. Huang, L. Chen, Interface Concentrated-Confinement Suppressing Cathode Dissolution in Water-in-Salt Electrolyte, *Adv. Energy Mater.* 10 (2020) 2000665.
- [105] J. Chen, C. Liu, Z. Yu, J. Qu, C. Wang, L. Lai, L. Wei, Y. Chen, High-energy-density aqueous sodium-ion batteries enabled by chromium hexacyanochromate anodes, *Chem. Eng. J.* 415 (2021) 129003.
- [106] X. Bu, L. Su, Q. Dou, S. Lei, X. Yan, A low-cost “water-in-salt” electrolyte for a 2.3 V high-rate carbon-based supercapacitor, *J. Mater. Chem. A*. 7 (2019) 7541–7547.
- [107] M. Pang, S. Jiang, J. Zhao, S. Zhang, R. Wang, N. Li, R. Liu, Q. Pan, W. Qu, B. Xing, “Water-in-salt” electrolyte enhanced high voltage aqueous supercapacitor with carbon electrodes derived from biomass waste-ground grain hulls, *RSC Adv.* 10 (2020) 35545–35556.
- [108] J. Kasnatscheew, M. Evertz, R. Kloepsch, B. Streipert, R. Wagner, I. Cekic Laskovic, M. Winter, Learning from Electrochemical Data: Simple Evaluation and Classification of LiMO₂-type-based Positive Electrodes for Li-Ion Batteries, *Energy Technol.* 5 (2017)

1670–1679.

- [109] A. Eftekhari, Energy efficiency: a critically important but neglected factor in battery research, *Sustain. Energy Fuels*. 1 (2017) 2053–2060.
- [110] M. Karlsmo, R. Bouchal, P. Johansson, High-performant all-organic aqueous sodium-ion batteries enabled by PTCDA electrodes and a hybrid Na/Mg electrolyte, *Angew. Chemie Int. Ed.* (2021).
- [111] T. Norgate, N. Haque, Using life cycle assessment to evaluate some environmental impacts of gold production, *J. Clean. Prod.* 29–30 (2012) 53–63.
- [112] S. Middlemas, Z.Z. Fang, P. Fan, Life cycle assessment comparison of emerging and traditional Titanium dioxide manufacturing processes, *J. Clean. Prod.* 89 (2015) 137–147.
- [113] F. Gao, Z. Nie, D. Yang, B. Sun, Y. Liu, X. Gong, Z. Wang, Environmental impacts analysis of titanium sponge production using Kroll process in China, *J. Clean. Prod.* 174 (2018) 771–779.
- [114] M.J. Eckelman, Facility-level energy and greenhouse gas life-cycle assessment of the global nickel industry, *Resour. Conserv. Recycl.* 54 (2010) 256–266.
- [115] B. Augustine, K. Remes, G.S. Lorite, J. Varghese, T. Fabritius, Recycling perovskite solar cells through inexpensive quality recovery and reuse of patterned indium tin oxide and substrates from expired devices by single solvent treatment, *Sol. Energy Mater. Sol. Cells*. 194 (2019) 74–82.
- [116] S. V. Joshi, L.T. Drzal, A.K. Mohanty, S. Arora, Are natural fiber composites environmentally superior to glass fiber reinforced composites?, *Compos. Part A Appl. Sci. Manuf.* 35 (2004) 371–376.
- [117] D. Bresser, D. Buchholz, A. Moretti, A. Varzi, S. Passerini, Alternative binders for sustainable electrochemical energy storage – the transition to aqueous electrode processing and bio-derived polymers, *Energy Environ. Sci.* 11 (2018) 3096–3127.
- [118] Data overview - International Energy Agency. <https://www.iea.org/data-and-statistics> (accessed November 3, 2021).